Supplement of Atmos. Chem. Phys., 24, 9975–10000, 2024
https://doi.org/10.5194/acp-24-9975-2024-supplement

Supplement of

Tropical tropospheric ozone distribution and trends from in situ and satellite data

Audrey Gaudel et al.

Correspondence to: Audrey Gaudel (audrey.gaudel@noaa.gov)

Supplementary Material

Section S1. Sampling sensitivity test for in-situ measurements

Even though high temporal and spatial variability in ozone is well recognized, the positive impact of abundant sample sizes on detectability of trends is often under-appreciated. In terms of detecting trends in the free troposphere several previous studies concluded that a sampling frequency of once per week generally fails to produce accurate monthly mean and trend values (Logan, 1999; Saunois et al., 2012; Chang et al., 2020).

Since the in-situ sampling scheme is infrequent and sporadic at most locations in this study, we use the IAGOS dataset collected above Africa which has the highest measurement density (more than 30 profiles in some individual months) to explore the impact of sample size on trend detection in the tropics. In order to provide a baseline reference at northern mid-latitudes, we also analyze the IAGOS data collected above Frankfurt, Germany. Table S2 provides monthly sample sizes from Africa and Frankfurt. Even though Africa has the most abundant IAGOS data in the tropics, the overall sample sizes are still small compared to Frankfurt. The following analysis focuses on observations in the free troposphere (700-300 hPa).

We compute mean absolute percentage error (MAPE) between the ozone trend inferred from the complete data record and from an ensemble of trend estimates for randomly subsampled data sets. As in Chang et al. (2020), trend estimates are defined as accurate once MAPE falls below 5% with increasing sampling frequency r. Table S3 provides the MAPE obtained from 1000 random subsamples composed of a fixed number of r profiles per month. The sampling strategy can be summarized as follows: if a given month has n profiles and the requested monthly sampling frequency is r, then 1) if $n \leq r$, we select all the profiles, this is fixed in each iteration; 2) if $n > r$, we select r profiles randomly in each iteration. From the table we see that 19 profiles per month are required to produce an accurate trend estimate over Frankfurt, which is consistent with Chang et al. (2020). However, over Africa, the decrease of the trend MAPE is slow and MAPE remains high even when the considered sampling frequency is increased because there is a sufficient number of IAGOS profiles (n>r) for just a small fraction of individual months.

The above finding is limited by the fact that we cannot meet the predetermined criterion for most cases in Africa (and the 5% criterion cannot be met). To determine the threshold for minimum sampling frequency for basic trend detection in the tropics, we further investigate the relationship between the magnitude of trends and the sampling frequency. In this case, basic trend detection refers to enough profiles to determine if there is a trend at a 2-sigma level, based on either the interquartile range (i.e. the 75% percentile) or tail (i.e. the worst-case scenario) of the sampling distribution, but it is not ideal for an accurate trend quantification. Figure S2 shows the distribution of median trends for a sampling frequency of 2, 4, 6, 8, 10 and 12 profiles a month, from 800 to 300 hPa with a 50 hPa vertical resolution. We can see the range of sampled trends becomes smaller when the sampling frequency is increased. Figures S2 and S3 show how the signal-to-noise ratios (i.e the ratio between the trend value and its uncertainty) of sampled trends vary with different sampling frequencies at 800 to 300 hPa. These figures reveal many considerations regarding the relationship between sampling frequency and the magnitude of trends:

1. If the magnitude of the trend is strong (e.g. > 3 nmol mol^{-1}/decade at 800 hPa), the trend can be detected at a low sampling frequency: 2 and 6 profiles per month are required for basic trend detection in 75% samples and the worst-case scenario (i.e. even for the worst case, the trend can be detected), respectively.
2. If the magnitude of the trend is moderate (e. g. between 1 and 2 nmol mol^{-1}/decade at 600 hPa):
   7 and 15 profiles per month are required for basic trend detection in 75% samples and the worst-case scenario, respectively.
3. If the trend is weak (e.g. around 1 nmol mol^{-1}/decade at 700 hPa), a high sampling frequency is required to detect the weak signal: 14 profiles per month are required for basic trend detection in 75% samples, and the worst-case scenario cannot be prevented in this analysis.
4. For pressure surfaces with weak and highly uncertain trends (e.g. 350 and 500 hPa, Figure S1), the same conclusion can be generally drawn at either low or high sampling rates.

Based on the above discussion, a typical sampling frequency of once per week is only sufficient for detection of very large trends (e.g. > |3| nmol mol^{-1}/decade), which are not common in the free troposphere. We also conclude that a sampling frequency of 7 profiles per month is sufficient for basic trend detection of tropospheric ozone in the tropics, when the magnitude of a trend is above |1| nmol mol^{-1}/decade, but additional data are required for accurate quantification. It should be noted that natural variability also plays a role in trend detection and attribution, but its impact is expected to be more pronounced when we conduct sensitivity analyses on varying lengths of the data record, which is beyond the scope of the current analysis. Even though the influence between natural variability and sampling frequency is typically inseparable, by focusing on the same data set and same data length, the impact of natural variability should be weak on this sensitivity analysis. In monitoring long-term changes, the first problem is to detect a trend (as we investigated in this analysis). Once the presence of a trend is established, any additional information will help us to improve the accuracy and precision of trend detection.

Section S2. Analysis steps for data fusion methodology

The features of our data fusion are, (i) to consider systematic ozone variability across vertical profile time series, instead of treating observations at different pressure surfaces as a set of independent time series. By taking account of the vertical correlation, the method produces more consistent trend estimates vertically, and the uncertainty can be effectively reduced; and (ii) to use the inverse of the (monthly) squared standard error as the weight when combining different sources of data records, so a record with a higher sampling frequency and/or lower variability has a higher influence. Analysis steps for data fusion can be described as follows (also described in Chang et al.(2022)):

For each data set and pressure surface (at 10 hPa vertical resolution), the time series is deseasonalized into data anomaly series, by using four harmonic functions. Explicitly, the anomalies are calculate by

$$y - a_0 - a_1 sin(Month \times \pi/6) - a_2 cos(Month \times \pi/6) - a_3 sin(Month \times \pi/3) - a_4 cos(Month \times \pi/3)$$

1. where y is the ozone value, and $(a_0, \dots, a_4)$ are coefficients to determine the seasonal cycle (see Chang et al. (2023) for implementation code).
2. For each data set and pressure surface, the anomaly series is standardized by dividing by its standard deviation, so the magnitude of data variability is similar between different pressure surfaces. The rationale of the regression problem is to find the best fit such that the sum of residuals is minimized. In terms of ozone profiles, ozone values in the upper troposphere are typically greater than the lower troposphere. Under this condition (since we consider vertical variability altogether), the statistical model prioritizes the reduction of fitted errors in the upper troposphere over the lower troposphere. Standardization removes this prioritization, and makes each vertical layer equally important across the troposphere. This consideration enables small scale variability to be better resolved by the statistical model.
3. Different sources of data records are combined by their normalized deviations (ND) , and implemented under the framework of generalized additive models (GAM) using R package mgcv (Wood, 2017). Based on the data preparation from the previous steps, the main syntax for GAM data integration in R can be demonstrated as follows:

```
> head(dt)
    Year Month index Pressure site Ozone_ppbv Ozone_ppbv_SE Ozone_anomaly_ppbv Ozone_standardized
248 1994     8     8      200    1   52.04750      9.643967        -0.07382282       -0.006870425
249 1994     8     8      210    1   46.90250      8.614597        -3.09289957       -0.312953398
250 1994     8     8      220    1   47.93800      7.589113        -1.12045218       -0.118577743
251 1994     8     8      230    1   46.49067      6.762999        -2.28952312       -0.245373816
252 1994     8     8      240    1   45.06875      6.251207        -3.52660169       -0.370912261
253 1994     8     8      250    1   44.44625      6.059981        -3.58347891       -0.391296508
> tail(dt)
      Year Month index Pressure site Ozone_ppbv Ozone_ppbv_SE Ozone_anomaly_ppbv Ozone_standardized
43014 2019    12   312      950    2   19.80000      11.63750          0.7552521         0.11666760
43015 2019    12   312      960    2   19.43333      11.70272          0.9353689         0.14621273
43016 2019    12   312      970    2   18.91667      11.89038          1.2253181         0.18773597
43017 2019    12   312      980    2   17.90000      12.27958          0.6877533         0.10584048
43018 2019    12   312      990    2   16.30000      13.05189         -0.3003434        -0.04605116
42929 2019    12   312     1000    2   14.43333      14.07423         -1.5527083        -0.22962453
> weights=(1/dt$Ozone_ppbv_SE^2)
> model=gam(Ozone_standardized ~ factor(site) + s(index, Pressure, bs="ds", k=2000), data=dt, weights=weights)
```

where 'index' is the monthly index spanned over the study period, and 'Pressure' is the observed pressure surface. This formulation indicates that, (i) temporal and vertical variabilities are modeled jointly (instead of two independent terms, based on the generalized thin plate splines); and (ii) the model fit is weighted by data uncertainty. The results can then be extracted by using predict(model, type='terms').

It should be noted that in terms of data fusion, it is also interesting to study the remaining variability from each individual dataset, e.g., after separating regional variations from the data set, the local influence can thus be better understood. Nevertheless, in this study the number of datasets to be integrated is too few (only two or three) to identify the remainder in each dataset (Gomes, 2022). If sufficient datasets are available (e.g., five data sources), one can replace the term factor(site) with a more sophisticated representation:

```
ti(index, Pressure, site, bs=c("ds","fs"),d=c(2,1),k=c(300,5))
```

(see Wood (2017) for further details), so the remaining variability in each data source can be properly characterized.

4. The model produces fitted/fused monthly time series at each pressure layer. Trends can be estimated after the fitted values are transformed back to the units of ppbv (reversing the standardization). Further implementation details for trend analysis are described by Chang et al. (2023).

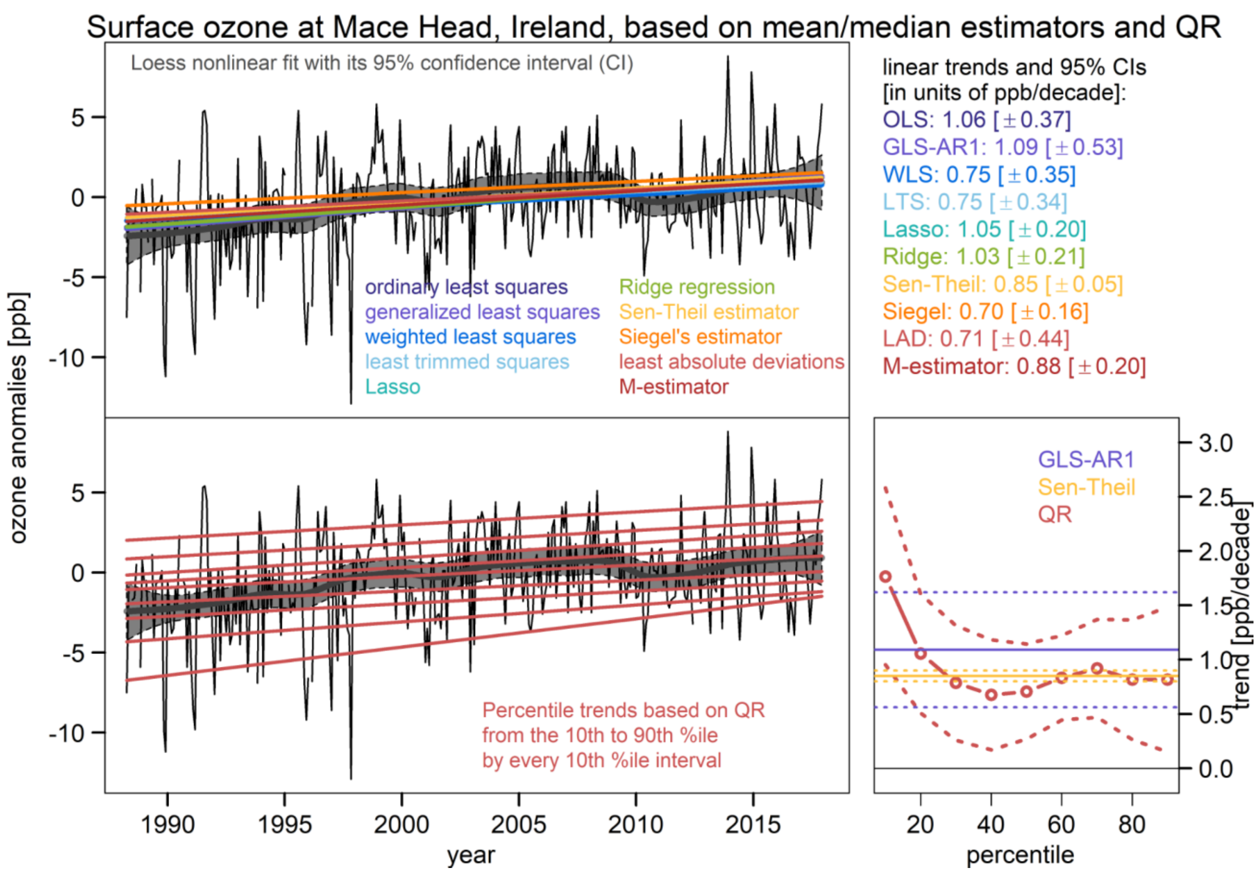

Figure 1 of Chang et al. (2023). A demonstration of the difference between a range of trend methods (upper panel) and percentile trends derived from quantile regression (QR, lower panel), based on surface ozone anomalies measured at Mace Head, Ireland (see Chang et al. (2023) for further details).

Section S3. Confidence scale for in situ trends

This section provides a detailed description of the factors taken into consideration when assigning a confidence level to the in situ ozone trends reported in Table 1.

- **Western Africa** (1994-2019): Data coverage is moderate (high sampling rate and moderate data gaps), combined with a low p-value associated with a strong trend, therefore **high confidence** is assigned to this region.
- **India** (1994-2019): Data coverage is moderate (moderate data gaps and moderate sampling rates), combined with a low p-value associated with a strong trend. According to Table A1, high confidence should be assigned. However, since both the number of data gaps and sampling rates are on the fuzzy area around our criteria between low and moderate data availability, **moderate confidence** is assigned to this region.
- **Samoa** (1994-2019): Data coverage is low (limited data gaps and low sampling rates), combined with a high p-value, so **very low confidence** is assigned to this region.
- **Natal + Ascension Island** (1994-2019): Data coverage is low (limited data gaps but low sampling rates), combined with a low p-value, so **moderate confidence** is assigned to this region.
- **Americas** (1994-2019): Data coverage is moderate (limited data gaps and moderate sampling rates), combined with a high p-value, so **low confidence** is assigned to this region.
- **Southeast Asia** (1994-2019): Data coverage is moderate (moderate data gaps and moderate sampling rate), combined with a low p-value, so **high confidence** is assigned to this region.
- **Malaysia/Indonesia** (1994-2019): Data coverage is low (moderate data gaps but low sampling rate), combined with a low p-value, so **moderate confidence** is assigned to this region.
- **Western Africa, India and Samoa** (2004-2019): Data coverage is low (short time period), combined with a high p-value, so **very low confidence** is assigned in these regions.
- **Natal + Ascension Island**, **Americas**, **Southeast Asia** and **Malaysia/Indonesia** (2004-2019): Data coverage is low (short time period), combined with a low p-value, so **moderate confidence** is assigned to these regions.

Section S4. The OMI/MLS measurements and drift corrections

The Ozone Monitoring Instrument (OMI) and Microwave Limb Sounder (MLS) are two of four instruments on board the Aura spacecraft which is flown in a sun-synchronous polar orbit at 705 km altitude with a 98.2° inclination. The Aura spacecraft was launched 15 July, 2004 and has an equatorial local crossing time of about 1:45 pm (ascending node). Both OMI and MLS instruments are still providing ozone measurements as of late 2023 which has yielded a nearly 20-year record of tropospheric ozone for evaluating global trends and other applications. In this study we focus on the 2004-2019 time period.

OMI/MLS tropospheric column ozone (TCO) is derived using the residual technique of Fishman et al. (1990). Fishman et al. (1990) originally subtracted Stratospheric Aerosols and Gas Experiment (SAGE) stratospheric column ozone (SCO) from Total Ozone Mapping Spectrometer (TOMS) total ozone measurements. We apply the same approach where Aura MLS SCO is subtracted from coincident Aura OMI total column ozone to derive TCO. The OMI/MLS algorithm is discussed in detail by Ziemke et al. (2006) and here we briefly summarize this method. First, along-track measurements of daily MLS profile ozone are vertically integrated in pressure from the top of the atmosphere down to the tropopause pressure to measure SCO. National Centers for Environmental Prediction (NCEP) re-analyses are incorporated for tropopause pressure using the standard World Meteorological Organization (WMO) 2K km^{-1} lapse-rate definition. Next, a spatial 2D (Gaussian + longitudinal) interpolation is used to fill in between the MLS SCO orbital-track measurements. Daily TCO is then determined by subtracting these SCO fields from OMI total column ozone fields. Finally, OMI/MLS TCO daily maps are averaged monthly to produce the final TCO product. The OMI/MLS product has a high sampling frequency, as shown in Figure S4 and Figure S5. Prior to 2009 each 5° x 5° grid cell had 300-500 measurements per month in the tropics; this number decreased to 200-400 measurements per month after the row anomaly took effect (described below). The measurement uncertainty (one standard deviation) of the OMI/MLS product is approximately 7 DU for a daily retrieval at 1° x 1.25° resolution, or approximately 2 DU at 5° x 5° resolution. It is reasonable to ask if this measurement uncertainty impacts the calculation of long-term trends from the OMI/MLS product. This question is addressed by the statistical field of error analysis (Grubbs, 1973; Taylor and Thompson, 1982; Moffat, 1988; Rabinovich, 2006; Buonaccorsi, 2010; Hughes and Hase, 2010). According to error analysis theory, if measurement uncertainty occurs randomly then the errors across a large sample size will cancel out and have little impact on the mean; in our case we are considering monthly mean values based on 200-400 OMI/MLS retrievals across a 5° x 5° grid cell. Given the very large sample size of the 5° x 5° OMI/MLS product the errors associated with measurement uncertainty cancel out and have little impact on the mean, and therefore little impact on the trend. Figure S6 below illustrates this concept using the ozonesondes above Debilt, The Netherlands (one profile per week), Uccle, Belgium (three profiles per week), and the IAGOS aircraft profiles above Europe (multiple profiles per day). All three data sets report clear positive trends for the period 1994-2019 based on monthly means produced from all available profiles (Figure S6a). In the next step random errors of 10% (representing measurement uncertainty) are imposed on all profiles. Figure S6b shows that the uncertainty of the monthly means increases slightly at Debilt and Uccle, but the uncertainty is almost unchanged for the IAGOS ensemble (due to the far greater sampling rates); the trend values at all three locations are almost unchanged, with only very slight increases in the 95% confidence intervals and p-values. In the final step random errors of 20% are imposed on all profiles (Figure S6c). These errors produce greater uncertainty of the monthly means for all three records, but the impact is greatest at Debilt which has the lowest sampling rate. Even though the imposed errors are relatively high, the overall trend values remain almost unchanged. The uncertainty of the trend values increases at all three sites, but the p-values remain below 0.05, and the impact is least for the IAGOS ensemble.

The OMI/MLS TCO measurements over time have encountered instrument drift and other long term quality issues including an OMI row-anomaly which became a large problem in late January 2009 and which still continues (Torres et al., 2018, and references therein). The row anomaly was caused by a physical obstruction in the optical path of the OMI instrument, resulting in about 1/3 of pixel measurements being flagged for non-use beginning in January 2009. Ziemke et al. (2019) discusses previous ozonesonde evaluation of offset and drift/row anomaly corrections for the OMI/MLS TCO product. For that study corrections were made to include a mean +2 DU offset adjustment and a global -1.0 DU decade^{-1} drift adjustment.

We have recently made a further adjustment to the OMI/MLS TCO long record guided by comparisons with ozonesondes, ground-based Brewer/Dobson total ozone, and OMI convective cloud differential (CCD) tropical TCO measurements. This new drift adjustment for OMI/MLS TCO begins by comparing OMI/MLS and ozonesonde daily TCO for October 2004-December 2019. The ozonesondes used for this analysis are from the Southern Hemisphere Additional OZonesondes (SHADOZ) network (Thompson et al. 2017; Witte et al. 2017, 2018; Sterling et al., 2017) and measurements from the World Ozone and Ultraviolet Radiation Data Center (WOUDC) and Network for the Detection of Atmospheric Composition Change (NDACC) (deMazière et al., 2018).

Figures S7, S8, and S9 show time series of OMI/MLS and sonde daily TCO for the NH, tropics, and SH, respectively. Printed in each panel (in red) is a calculated linear fit of OMI/MLS minus sonde TCO where only coincident daily measurements were included. We chose sonde sites that had the most coverage over the long record. Because we collocate daily OMI/MLS and sondes for the line-fit analysis, we use all available sonde measurements even if there is as little as only one sonde measurement per month on average. In the NH (Figure S7) the mean drift difference of OMI/MLS minus sonde TCO is calculated to be +0.54 ± 0.64 DU decade^{-1}. For the tropics (Figure S8) the mean drift difference is +0.57 ± 0.40 DU decade^{-1}. In the SH (Figure S9) the mean drift difference is +1.33 ± 0.98. From these results, we subjectively applied a new overall correction to OMI/MLS TCO of -0.6 DU decade^{-1} everywhere at all latitudes and longitudes.

After combining this -0.6 DU decade^{-1} correction with the previous -1 DU decade^{-1} correction, the total drift correction is now equivalent to about -3 DU total change over the long record. This overall -3 DU drift correction coincides closely with calculated drift error for OMI total ozone of about +3 DU (+1%) from ground-based Brewer and Dobson total ozone comparisons (e.g., Figure S10 from G. Labow, personal communication, 2023). As an additional cross-check for the new adjustment, we also included comparisons with OMI CCD tropical TCO (Ziemke et al., 1998) as shown in Figure S11; this suggested an additional drift correction of about -0.5 ± 0.30 DU decade^{1} which is comparable to the ozonesonde comparisons. Thus, all three of these analysis methods (sondes, ground total ozone, CCD) for evaluating positive drift in OMI/MLS TCO agree.

Section S5. Tables and Figures

Table S1. Description of IAGOS fleet with the airlines, airports and number of profiles for the three focus time periods in this study (1995-2019 for long-term trends calculation, 2004-2019 for satellite evaluation, and 2014-2019 for present-day ozone distribution). All data above all airports listed in the table are used to quantify the distribution and trends of tropical tropospheric ozone as well as the evaluation of the satellite data.

Region	Airline	Airport	N profiles [1995-2019]	N profiles [2004-2019]	N profiles [2014-2019]
Americas	Austrian	Punta Cana	11	0	0
	Lufthansa Air France	Bogota	560	356	347
	Lufthansa Air France	Saint Martin	89	75	32
	Lufthansa	Panama City	14	14	14
	Iberia Lufthansa	Guayaquil	4	2	2
	Lufthansa Air France	Lima	24	0	0
	Lufthansa	Maracay	1	0	0
	Lufthansa	San Juan	45	0	0
	Lufthansa	Antigua	31	0	0
	Iberia Lufthansa	San Jose	32	32	32
	Lufthansa Air France	Caracas	1214	633	85
	Lufthansa Air France	Mexico City	52	3	3
	Air France	Cayenne	216	0	0
	Lufthansa Air France	Quito	72	1	1
	Lufthansa	Cali	2	0	0
	Air France	Recife	25	0	0
	Lufthansa	Santo Domingo	2	0	0
	Lufthansa	Porlamar	2	0	0
	Austrian	Puerto Plata	12	0	0
	Lufthansa Air France	Malabo	182	182	182
	Air France	Yaounde	47	16	6
	Lufthansa Air France	Libreville	31	5	2
	Lufthansa Air France	Abuja	376	355	351

	Air France	Ndjamena	25	25	23
	Air France Lufthansa Sabena	Abidjan	233	38	35
	Air France	Bamako	48	48	40
	Sabena Lufthansa Air France	Lagos	761	441	396
	Air France	Ouagadougou	122	113	74
	Lufthansa	Tahoua	2	2	2
	Air France	Djibouti	11		9
	Lufthansa Air France	Port Harcourt	190	188	185
	Air France Lufthansa Sabena	Dakar	101	12	0
	Lufthansa	Bamenda	1	1	1
	Sabena	Entebbe	75		0
	Air France	Nouakchott	91	62	58
	Lufthansa	Khartoum	272		14
	Air France Air Namibia Lufthansa	Accra	139	66	43
	Air France	Niamey	123	113	56
	Lufthansa Air France	Freetown	22	22	18
	Lufthansa	Jeddah	95		95
	Sabena Air France	Douala	215	87	53
	Sabena Air France	Lome	103	72	58
	Sabena Air France	Cotonou	104	76	68
	Air France Lufthansa Sabena	Conakry	74	49	45
	Air France	Pointe-noire	28	28	28
	Sabena	Kigali	64		0
	Air Namibia Air France	Brazzaville	40	31	29
	Air France Sabena	Kinshasa	102	19	17

	Lufthansa	Luanda	254	210	89
	Air Namibia				
	Air France				
India	Cathay Pacific	Chennai	680	437	209
	Lufthansa				
	Sabena				
	Air France	Bangalore	32	32	32
	Austrian	Male	80	4	4
	LTU				
	Lufthansa				
	Austrian	Colombo	58	19	19
	Lufthansa				
	LTU				
	Austrian	Mumbai	177	56	28
	Cathay Pacific				
	Lufthansa				
	Air France				
	Cathay Pacific	Hyderabad	552	552	12
	Lufthansa				
Southeast Asia	Cathay Pacific	Cebu	18	18	18
	Lufthansa	Bangkok	1535	895	598
	Air France				
	Austrian				
	Cathay Pacific				
	China Airlines				
	China Airlines	Manila	191	191	146
	Austrian				
	Cathay Pacific				
	Lufthansa				
	China Airlines	Ho Chi Minh City	367	231	182
	Cathay Pacific				
	Lufthansa				

	Air France				
	China Airlines	Guam	8	8	8
	Cathay Pacific	Hong Kong	80	80	80
	China Airlines				
Malaysia/Indonesia	Lufthansa	Paya Lebar	1	0	0
	Austrian	Darwin	3	0	0
	China Airlines	Jakarta	113	86	61
	Cathay Pacific				
	Lufthansa				
	Air France				
	Cathay Pacific	Surabaya	18	18	18
	China Airlines				
	China Airlines	Kuala Lumpur	208	192	139
	Cathay Pacific				
	China Airlines	Denpasar	32	32	32
	Cathay Pacific				
	China Airlines	Singapore	265	143	92
	Cathay Pacific				
	Lufthansa				
	Air France				

Table S2. Number of IAGOS profiles by year and month above Africa (left panel) and Frankfurt, Germany (right panel).

	1	2	3	4	5	6	7	8	9	10	11	12
1997	0	0	0	6	52	37	48	65	40	58	28	8
1998	9	23	9	2	4	2	4	2	24	6	8	10
1999	22	18	13	15	12	20	32	8	2	30	15	12
2000	22	10	20	44	38	18	54	40	16	36	23	6
2001	18	14	32	66	0	0	0	4	2	29	10	12
2002	20	45	37	0	0	0	2	0	1	18	8	2
2003	19	32	4	14	30	12	38	47	42	66	46	10
2004	34	18	22	0	2	13	20	4	2	32	0	0
2007	12	6	0	0	0	0	0	0	0	0	0	4
2008	6	2	4	2	2	0	2	2	2	2	0	2
2009	8	2	22	4	0	0	8	0	0	0	0	0
2010	0	3	0	0	0	0	0	0	0	5	0	2
2011	0	4	6	0	0	0	21	2	4	2	6	10
2012	0	6	4	7	0	0	14	2	17	32	30	54
2013	70	21	21	8	0	33	34	6	2	29	32	36
2014	34	9	0	13	4	16	0	0	0	0	0	0
2015	0	4	14	44	38	0	10	19	38	56	33	68
2016	55	61	49	37	42	42	57	36	33	16	23	44
2017	62	40	18	54	80	86	51	60	86	38	56	19
2018	4	15	96	51	52	64	49	7	5	0	0	16
2019	6	14	28	24	28	31	29	30	24	28	24	14

	1	2	3	4	5	6	7	8	9	10	11	12
1994	0	0	0	0	0	0	0	62	101	96	98	116
1995	122	141	121	119	115	125	141	109	150	64	100	84
1996	139	123	39	123	153	128	121	158	101	102	145	103
1997	168	115	134	107	156	180	192	185	192	162	114	143
1998	185	146	158	137	165	126	121	187	181	160	141	143
1999	113	148	131	132	169	182	219	201	191	206	190	198
2000	177	163	172	218	209	167	196	168	151	155	135	131
2001	134	109	140	150	101	92	127	118	117	119	83	88
2002	68	109	104	46	45	13	74	96	117	126	130	57
2003	45	90	97	121	118	189	188	215	178	197	169	180
2004	158	128	136	112	108	172	212	184	111	126	58	142
2005	138	105	146	121	131	120	96	98	125	89	105	103
2006	71	68	73	70	78	78	129	83	109	117	113	116
2007	75	85	68	66	71	81	90	76	80	20	49	67
2008	80	67	56	29	69	78	54	70	64	70	88	115
2009	130	99	118	63	111	110	147	80	53	10	47	56
2010	9	46	6	2	4	4	4	4	15	40	49	54
2011	53	90	109	102	58	73	171	98	95	122	98	102
2012	16	63	85	138	38	13	110	86	104	79	109	145
2013	159	91	83	84	104	139	125	94	86	77	90	134
2014	109	85	71	126	103	132	104	63	36	55	36	10
2015	58	31	35	92	86	58	102	124	90	114	63	61
2016	64	74	52	95	148	111	150	145	120	89	85	135
2017	119	94	50	125	134	143	139	147	125	101	114	52
2018	46	23	66	62	78	89	85	59	42	51	0	47
2019	41	45	49	59	70	105	83	53	20	46	44	34

Table S3. The mean absolute percentage error (MAPE) values between the trend value derived from the full dataset and sampled trends are reported, based on quantile regression and free tropospheric observations (700-300 hPa) above Frankfurt and Africa. Sampled trends are generated by one thousand random samples for each of a predetermined number of profiles per month.

#profiles per month	1	2	3	4	5	6	7	8	9	10
Frankfurt	69.1	39.3	28.1	18.0	16.7	15.3	14.3	12.4	11.7	9.1
Africa	93.9	85.0	79.6	71.9	64.3	55.2	54.9	53.1	50.1	48.9
#profiles per month	11	12	13	14	15	16	17	18	19	20
Frankfurt	9.0	8.7	8.3	7.6	7.2	5.9	5.6	5.2	4.8	3.9
Africa	47.8	46.4	42.3	40.5	38.9	34.0	31.6	26.4	26.0	23.2

Table S4. Summary of the TTCO trends in nmol mol^{-1} decade^{-1} from IAGOS

The sampling column reports three numbers for the in situ data: i) the number on the top refers to the average number of profiles per months taking into account all the months with profiles, ii) the number in the middle refers to the percentage of months with data for the studied time-period (1994-2019 or 2004-2019), iii) the number in the bottom refers to the total number of profiles for the studied time period (1994-2019 or 2004-2019). We provide these numbers for a reference, but, for these three IAGOS regions, our final conclusions are based on the confidence scale for the fused (IAGOS + SHADOZ) results (See Table 1 in the main manuscript).

		1994-2019			2004-2019		
		Trends±2σ (nmol mol^{-1} decade^{-1})	p-value	Sampling	Trends±2σ (nmol mol^{-1} decade^{-1})	p-value	Sampling
IAGOS	Americas	2.07±0.51	<0.01	10.8 71.5% 2403	0.64±1.21	0.29	9.8 66.1% 1248
	Southeast Asia	4.66±0.46	<0.01	15.3 62.7% 2194	4.07±1.60	<0.01	16.2 61.1% 1423
	Malaysia/Indonesia	6.44±1.13	<0.01	8.0 44.4% 636	8.62±2.29	<0.01	9.3 47.2% 475

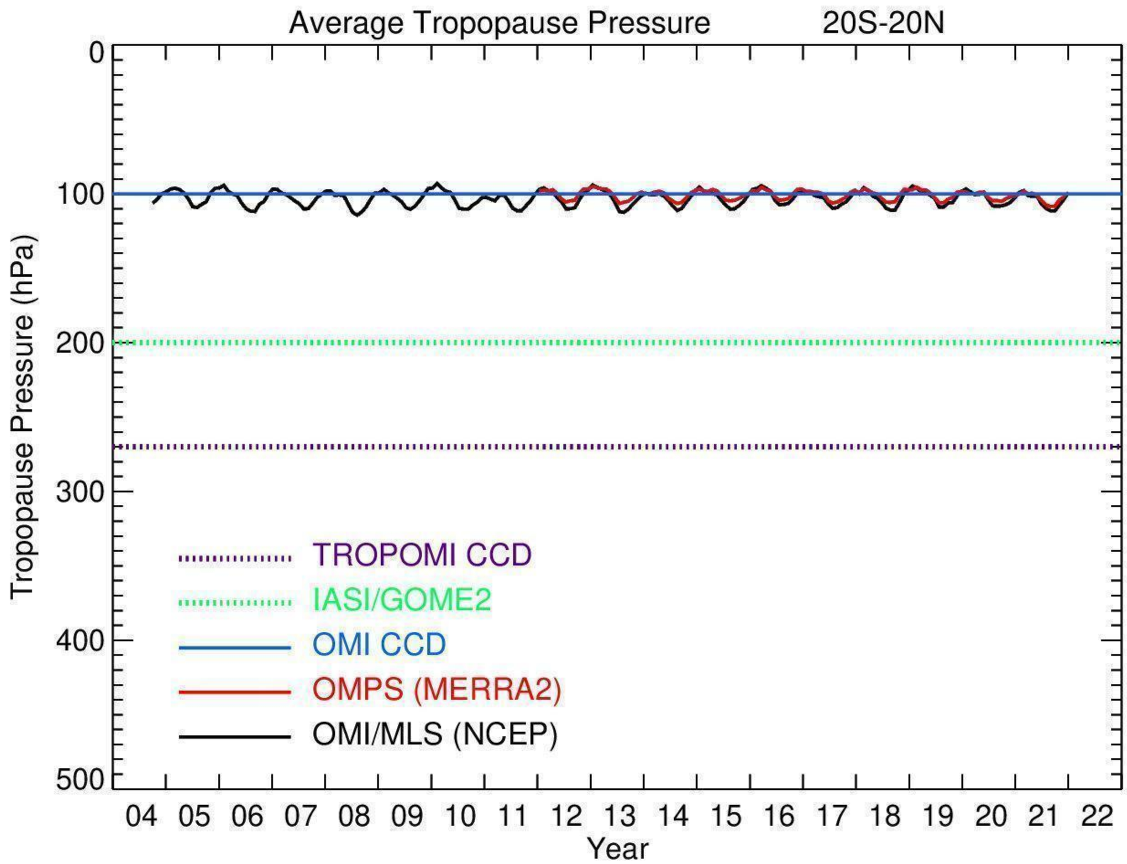

Figure S1. Time series of the monthly mean of the tropopause pressure level used to define the tropical tropospheric column ozone (TTCO) with satellite data.

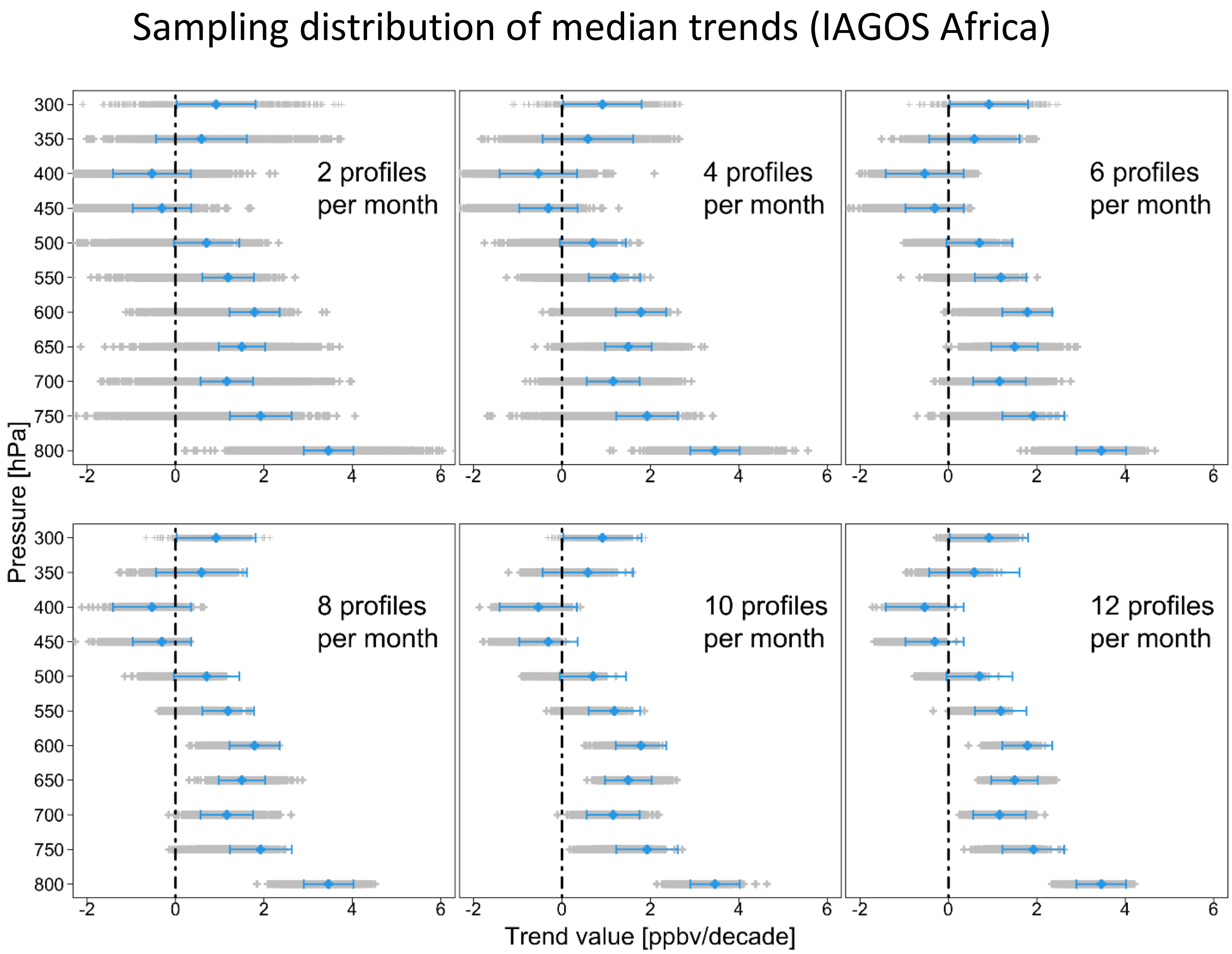

Figure S2. Sampling distributions of trends for a sampling frequency of 2 to 12 profile-per-month above Africa. The estimation is based on quantile regression. Blue diamonds are the median trend estimates derived from all available data, the horizontal blue bars indicate the 95% confidence interval of the trend with full sampling, each gray cross represents the estimate produced by a random sampling from 1000 iterations.

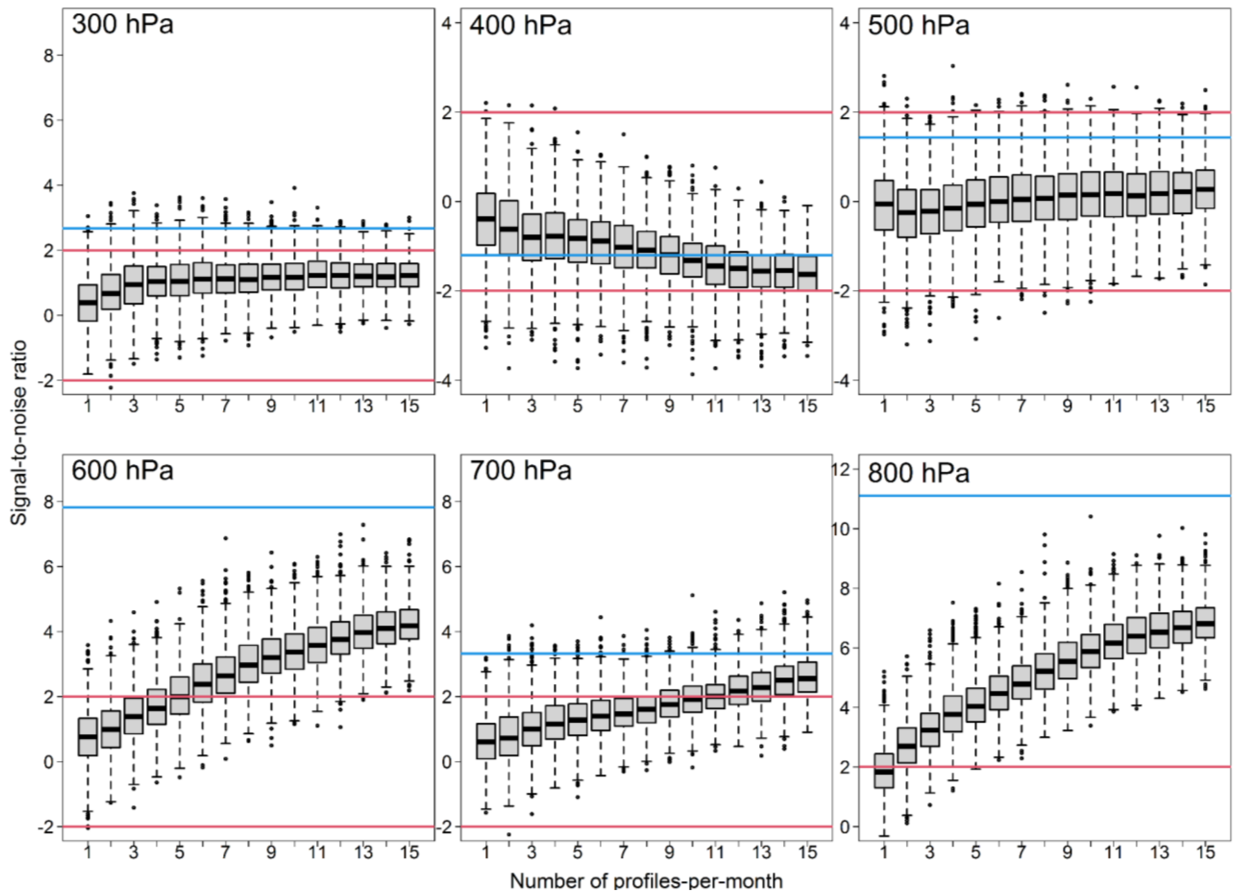

Figure S3. Sampled signal-to-noise ratios of the ozone trends. The ratios vary with different sampling frequencies at 800 to 300 hPa above Africa. Red lines (at signal-to-noise ratios of 2 and -2) represent the conventional trend detection threshold (i.e. 95% confidence level), and blue lines represent the SNR derived from all available data.

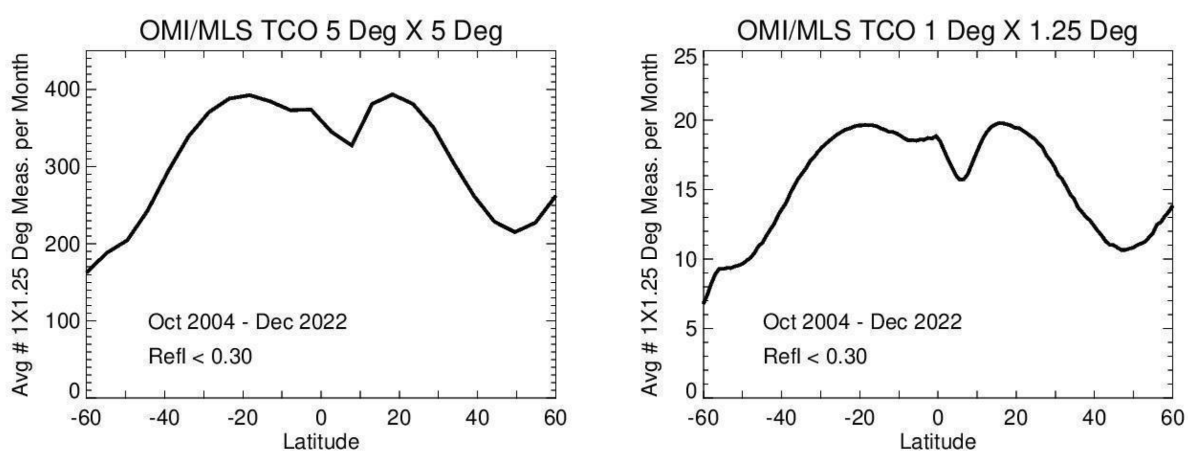

Figure S4. Number of 1° x 1.25° resolution OMI/MLS tropospheric column ozone measurements per month in a 5°x5° grid cell (left panel) or a 1° x 1.25° grid cell (right panel), by latitude. The data have been cloud-filtered using a low reflectivity threshold of R < 0.30, and the results are averaged across October 2004 to December 2022.

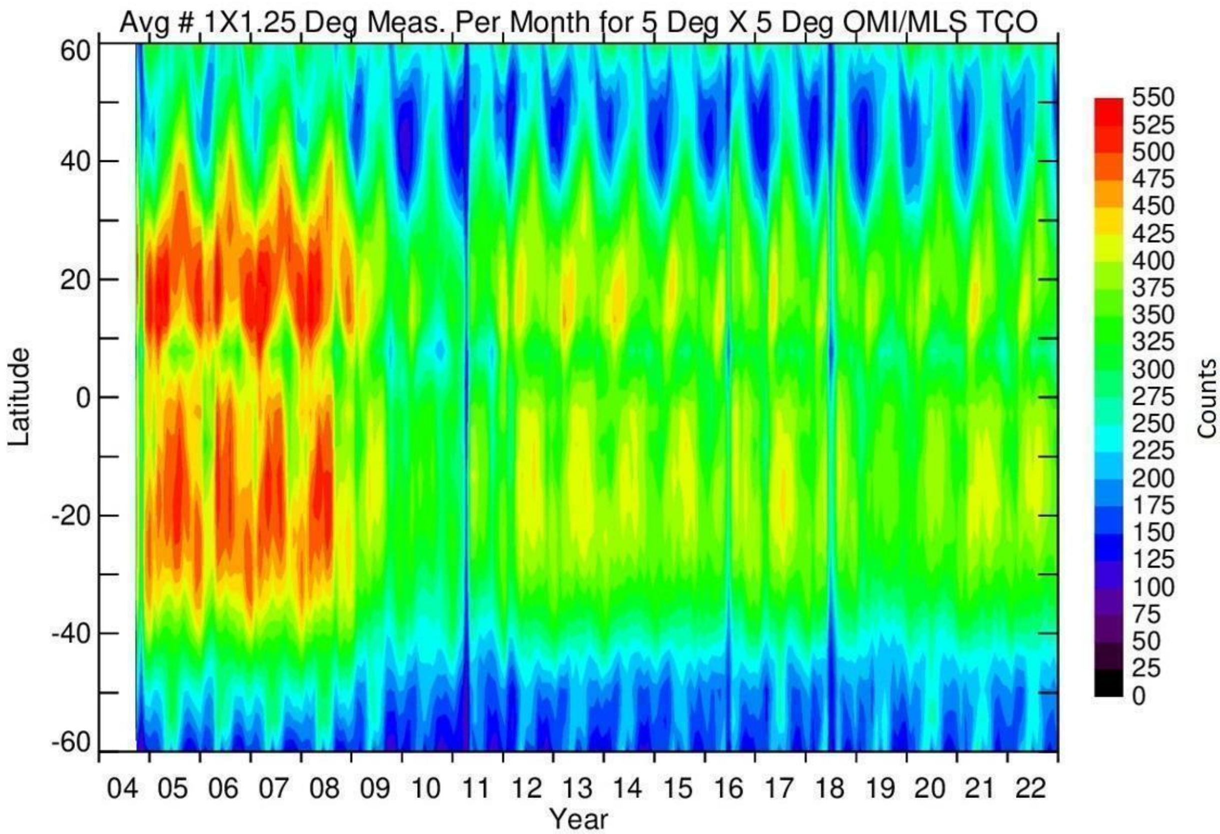

Figure S5. Hovmoller plot of average number of daily 1°x1.25° tropospheric column ozone (TCO) measurements per month within each 5°x5° grid cell, following R<0.30 cloud filtering. Starting January 2009 there are fewer measurements due to the row anomaly problem.

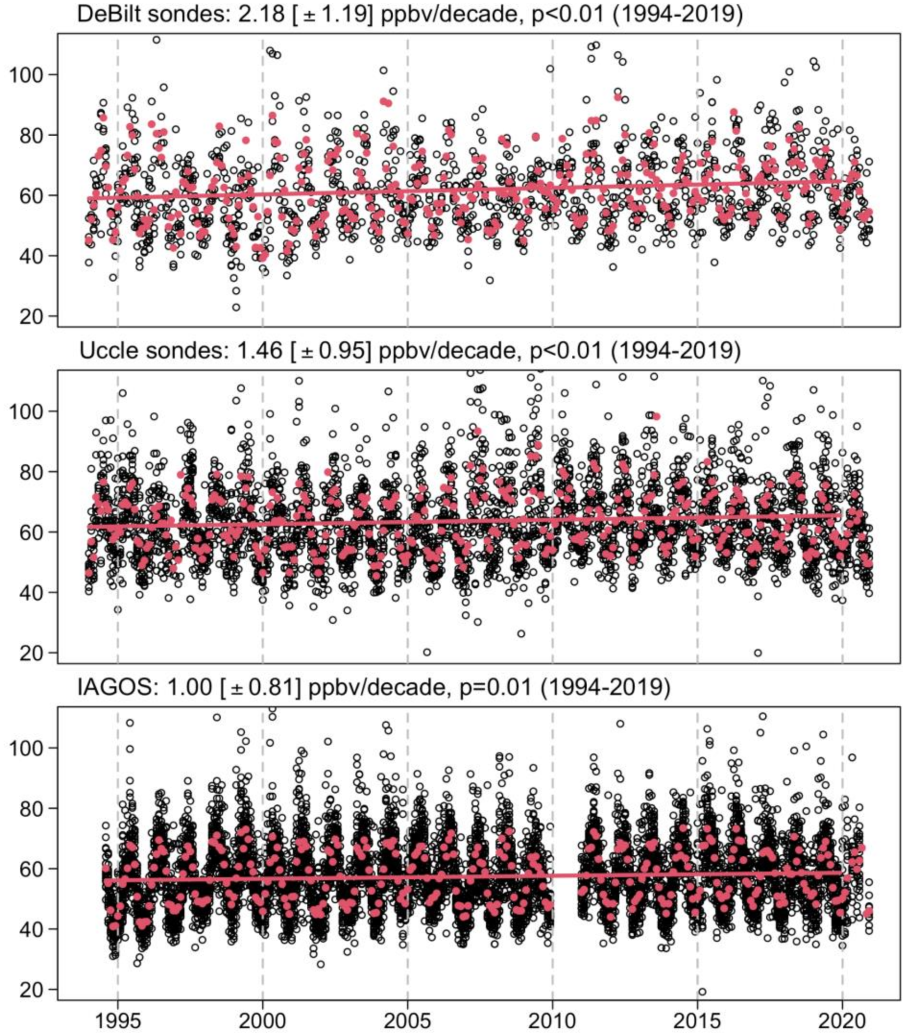

Figure S6a. Mid-tropospheric (700-300 hPa) ozone trends (1994-2019) at three European locations: Debilt, The Netherlands (top), Uccle, Belgium (center) and an ensemble of all IAGOS profiles above Europe (bottom). Each black point represents a mid-tropospheric observation (averaged over 700-300 hPa) from a single profile, while the red points represent monthly means (under the assumption of no measurement uncertainty). Also shown are the linear trends for 1994-2019, with 95% confidence intervals and *p*-values.

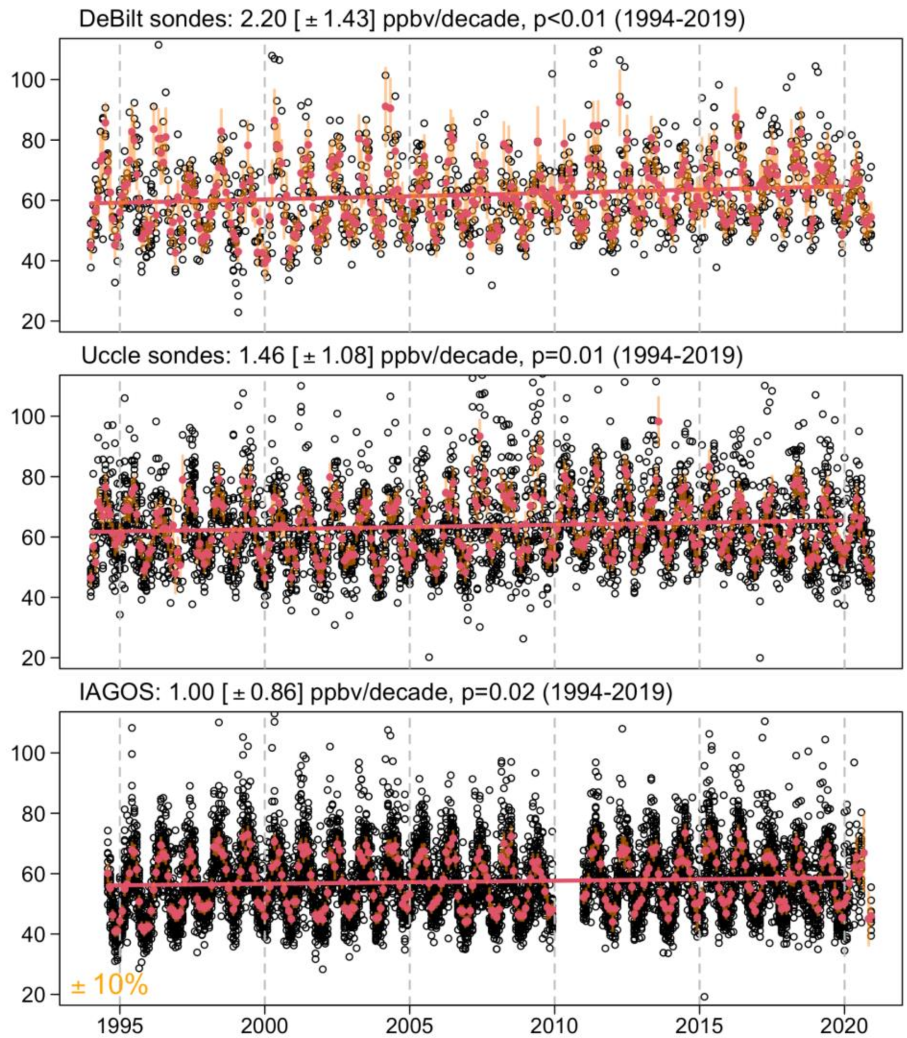

Figure S6b. As in Figure S6a, but with random noise of 10% imposed on each individual ozone value (the noise value is randomly selected from a normal distribution with 0 mean and SD as y*0.10 (e.g. for a desired uncertainty of ±10%)). For each month, monthly means are produced from the corresponding noise-added observations. This procedure is repeated 10,000 times, and the 2.5th and 97.5th percentiles from the 10,000 noise-added monthly means indicate the 95% confidence interval of the means (shown with the orange bars on each monthly mean). Finally, 10,000 trend values are produced, and the mean and standard deviation become the final trend and sigma uncertainty reported in each panel of the figure.

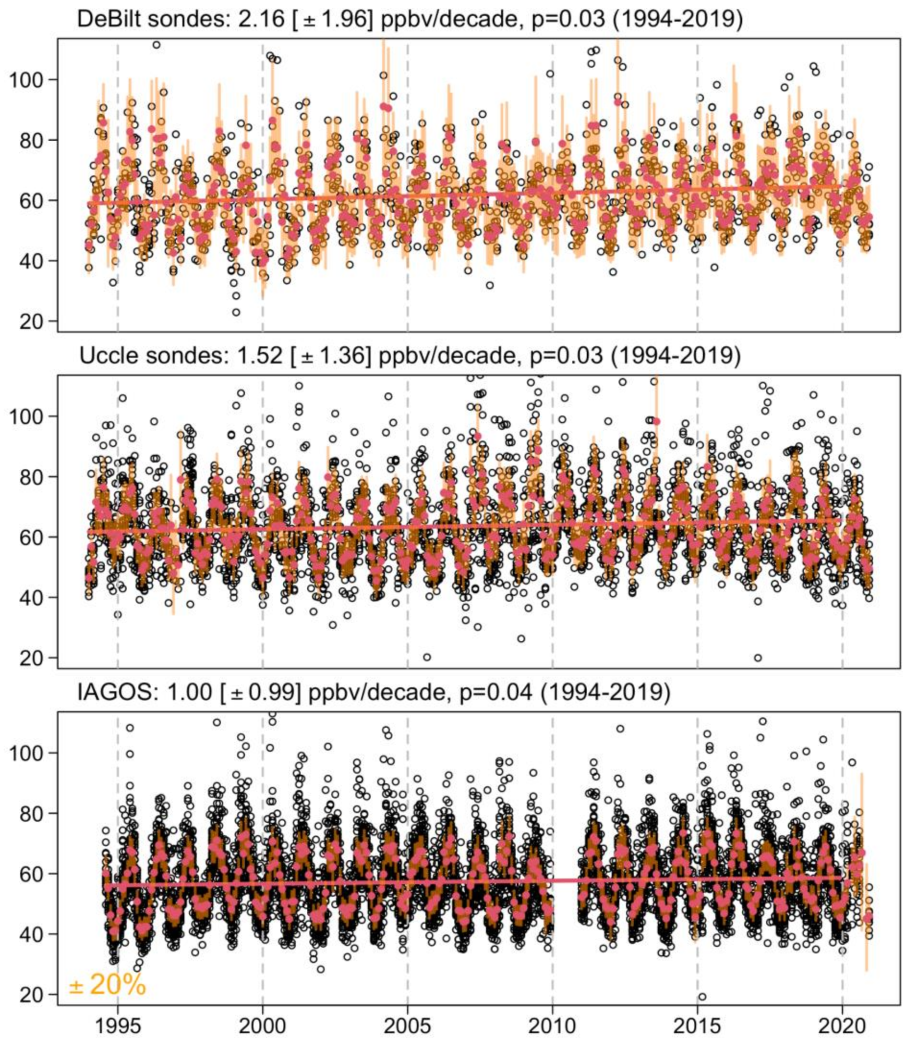

Figure S6c. As in Figure S6b but with 20% random noise imposed on each individual ozone value.

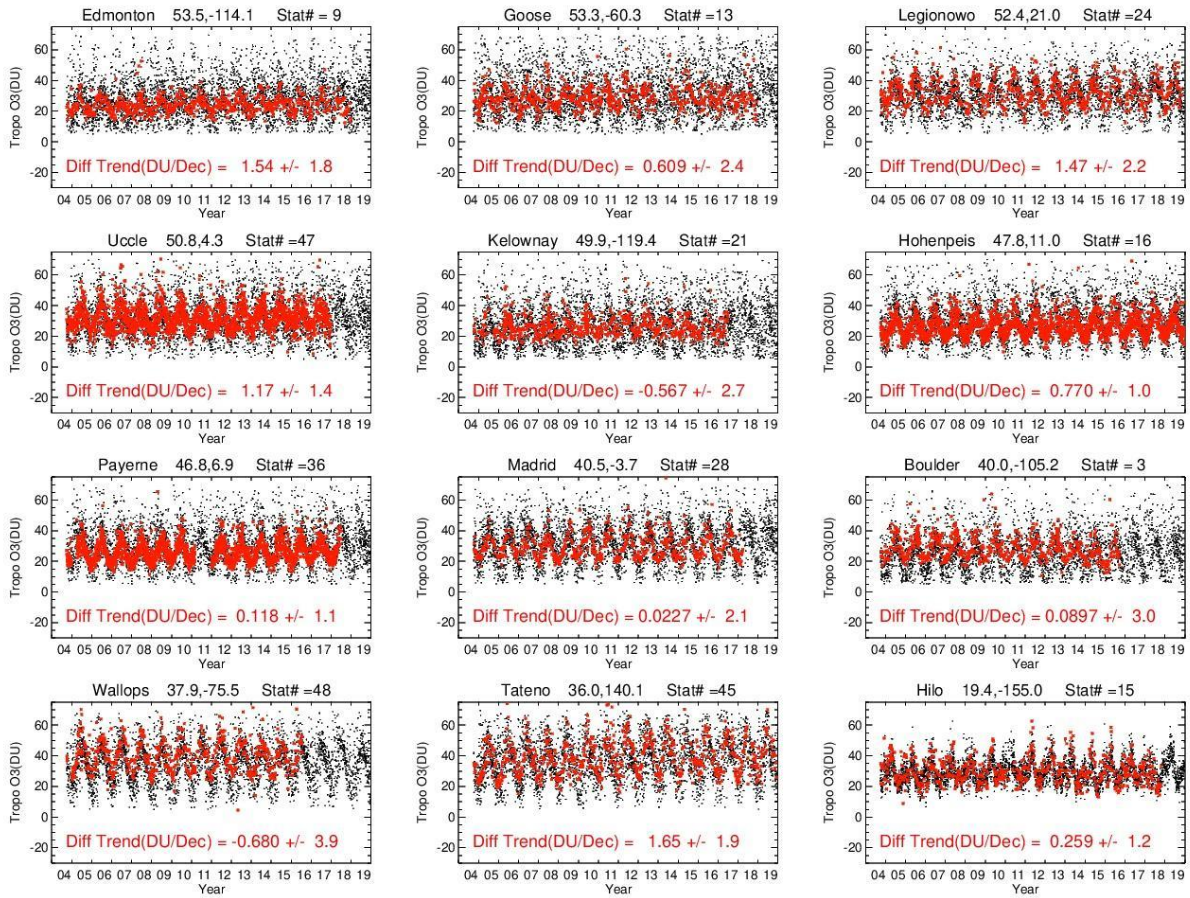

Figure S7. Daily time series of TCO (in DU) for OMI/MLS (black) and ozonesondes (red) for 2004-2019 from WOUDC and NDACC. Stations were selected (indicated) that exhibited the best coverage over the long record. Calculated drift difference of OMI/MLS TCO minus sonde TCO in DU decade^{-1} are also shown for each site (including 2σ uncertainty). Mean drift difference for the combined sites is $+0.54 \pm 0.64$ DU decade^{-1}.

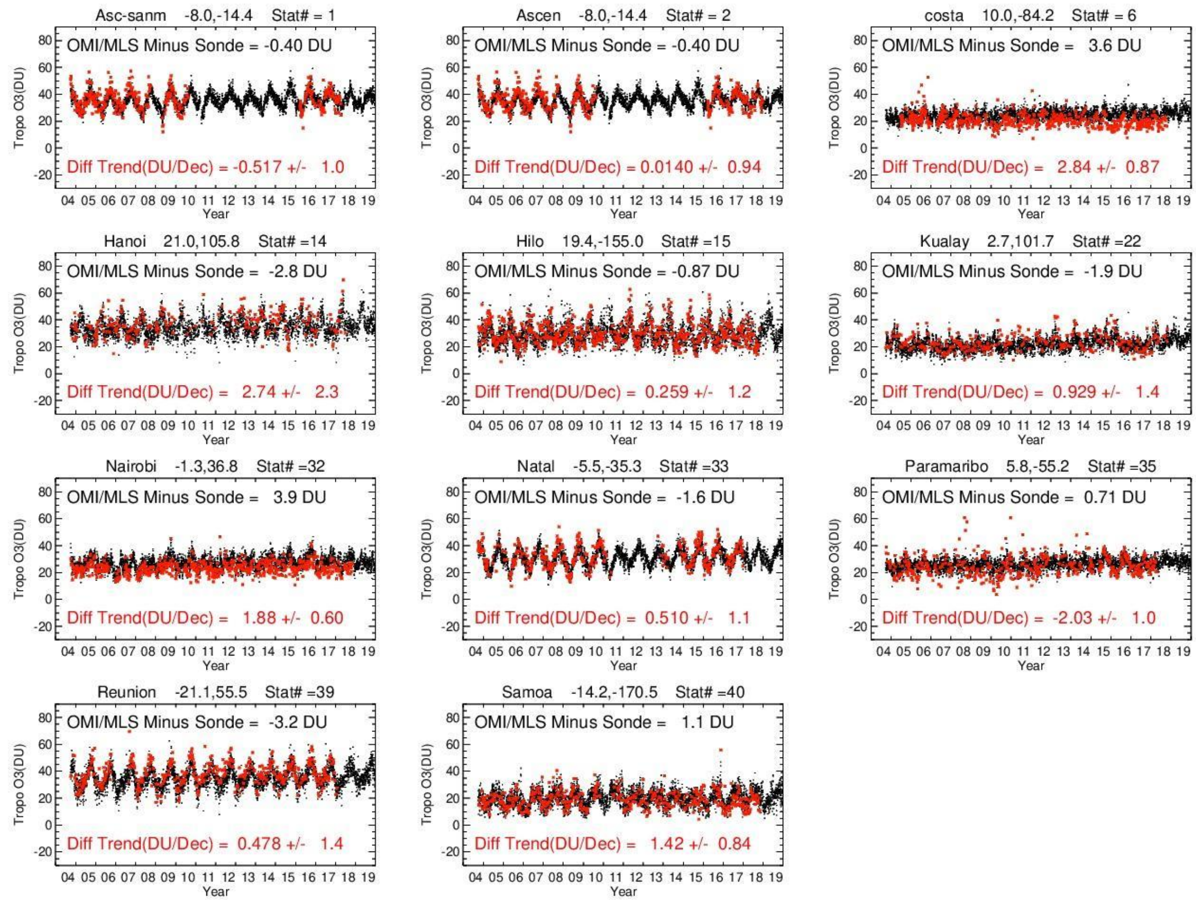

Figure S8. Similar to Figure S4.1, but for the tropics using SHADOZ data. Mean drift difference for the combined sites is +0.57 ± 0.40 DU decade^{-1}.

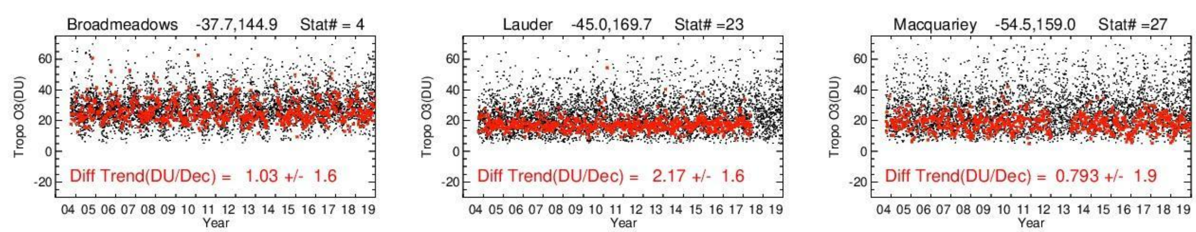

Figure S9. Similar to Figure S7, but for the SH. SH sonde measurement sites are sparse compared to the NH and tropics. Mean drift difference for these combined SH sites is +1.33 ± 0.98 DU decade^{-1}.

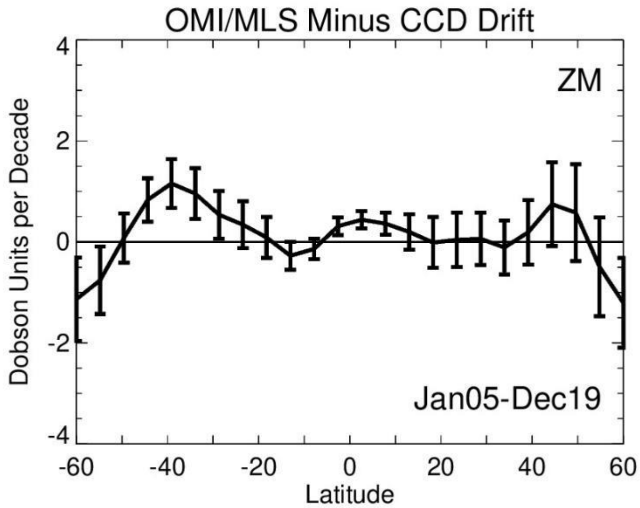

Figure S10. OMI/MLS TCO minus OMI CCD TCO coincident monthly differences (in DU) zonally averaged over the Pacific (120°W-120°E). The curve represents line-fits (including ± 2σ uncertainties) of monthly OMI/MLS minus CCD differences for 2005-2019.

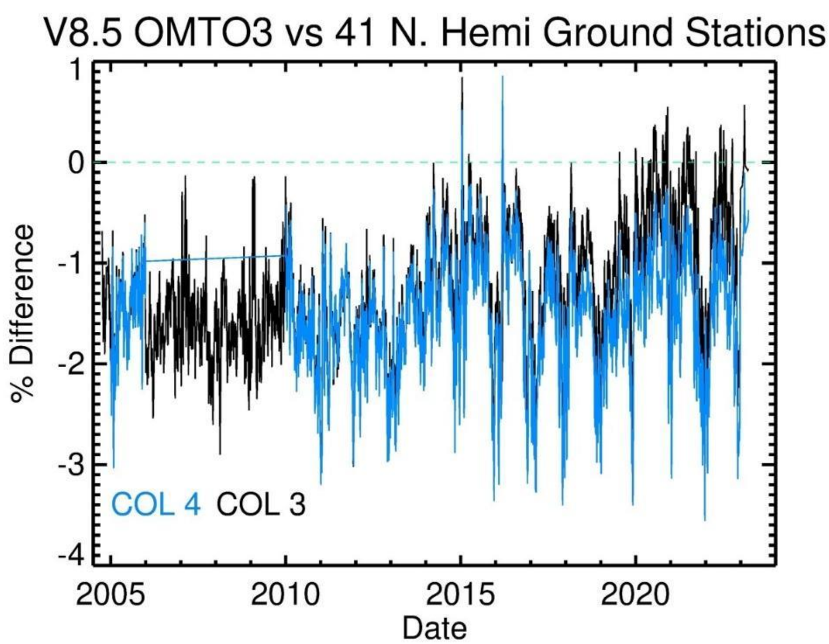

Figure S11. Public domain OMI v8.5 total ozone minus ground-based Dobson/Brewer total ozone differences in percent (Gordon Labow, personal communication, 2024). The black curve shows differences for v8.5 OMI total ozone using current collection-3 L1B data processing while the blue curve shows differences using OMI total ozone processed using a preliminary collection-4 L1b dataset. The collection-4 processing tends to reduce drift and other anomalies in

OMI total ozone and is work in progress. The black curve corresponds to the data that is currently used for the OMI/MLS TCO and shows obvious long-term drift changes going from about -1.5% to -0.5% over the almost 20-year record. We conclude from Figure S11 that the OMI total ozone has a positive drift of about +1% (or +3 DU) over the long record. This is the drift error in OMI total ozone inferred from the ground measurements, prior to any adjustments made for the OMI/MLS TCO.

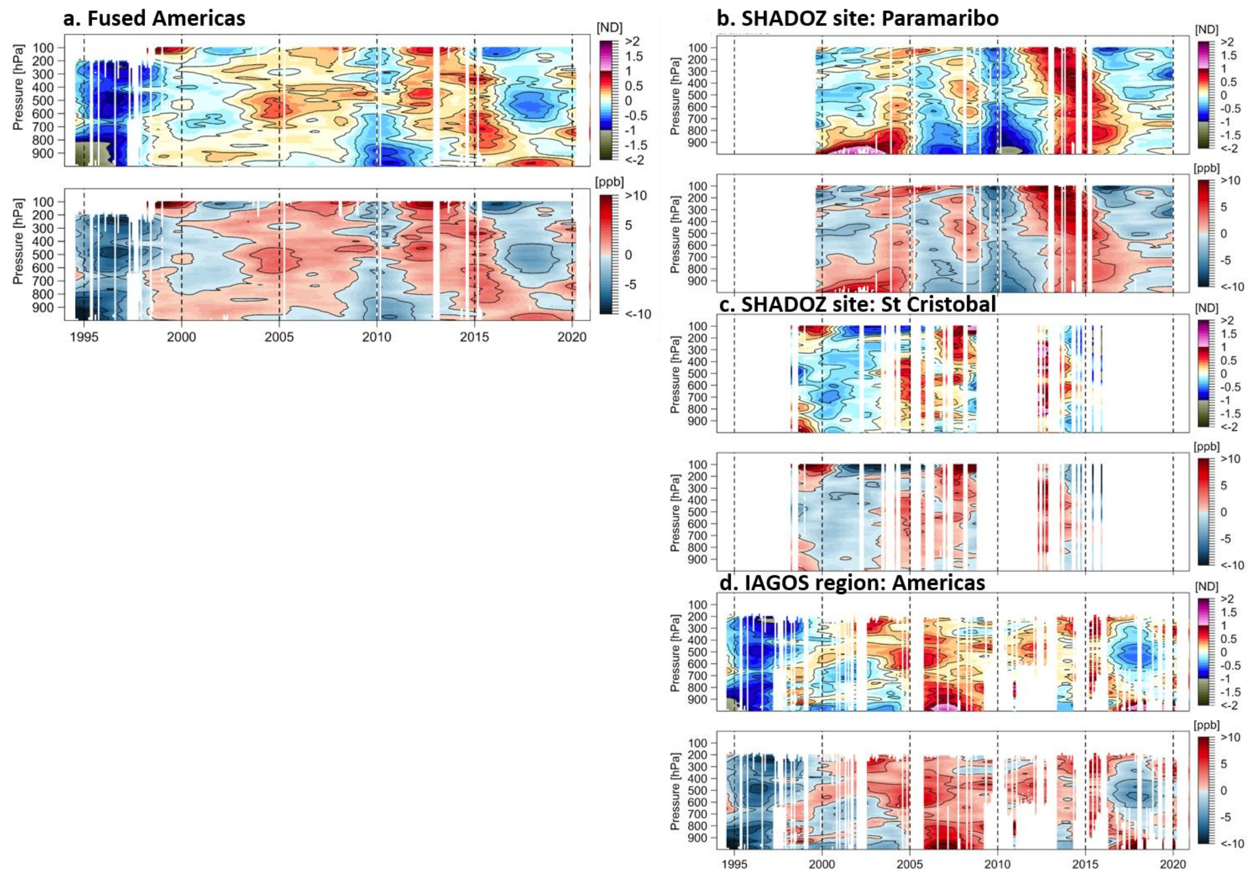

Figure S12. Ozone mean distributions above Americas based on normalized deviation (ND). Panels show the results of the fused data set from IAGOS and SHADOZ (a), and for the SHADOZ individual sites (Paramaribo and San Cristobal, panels b and c) and IAGOS region (Americas, panel d).

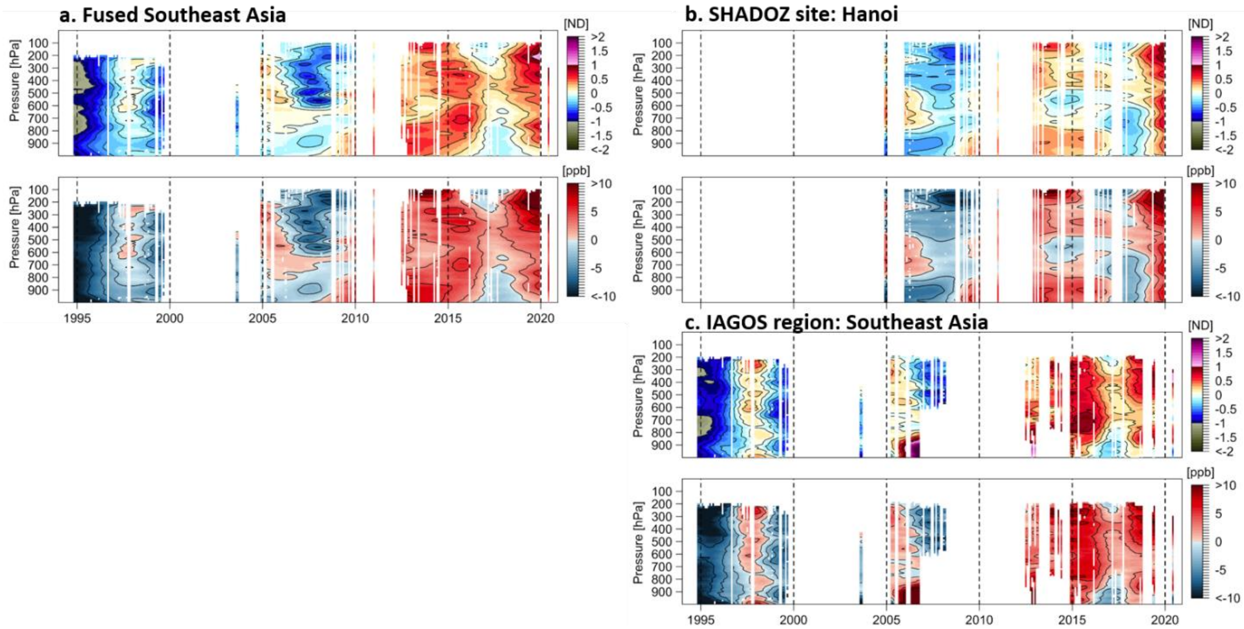

Figure S13. Same as Figure S12 but above Southeast Asia. The SHADOZ individual site used for the fused data is Hanoi.

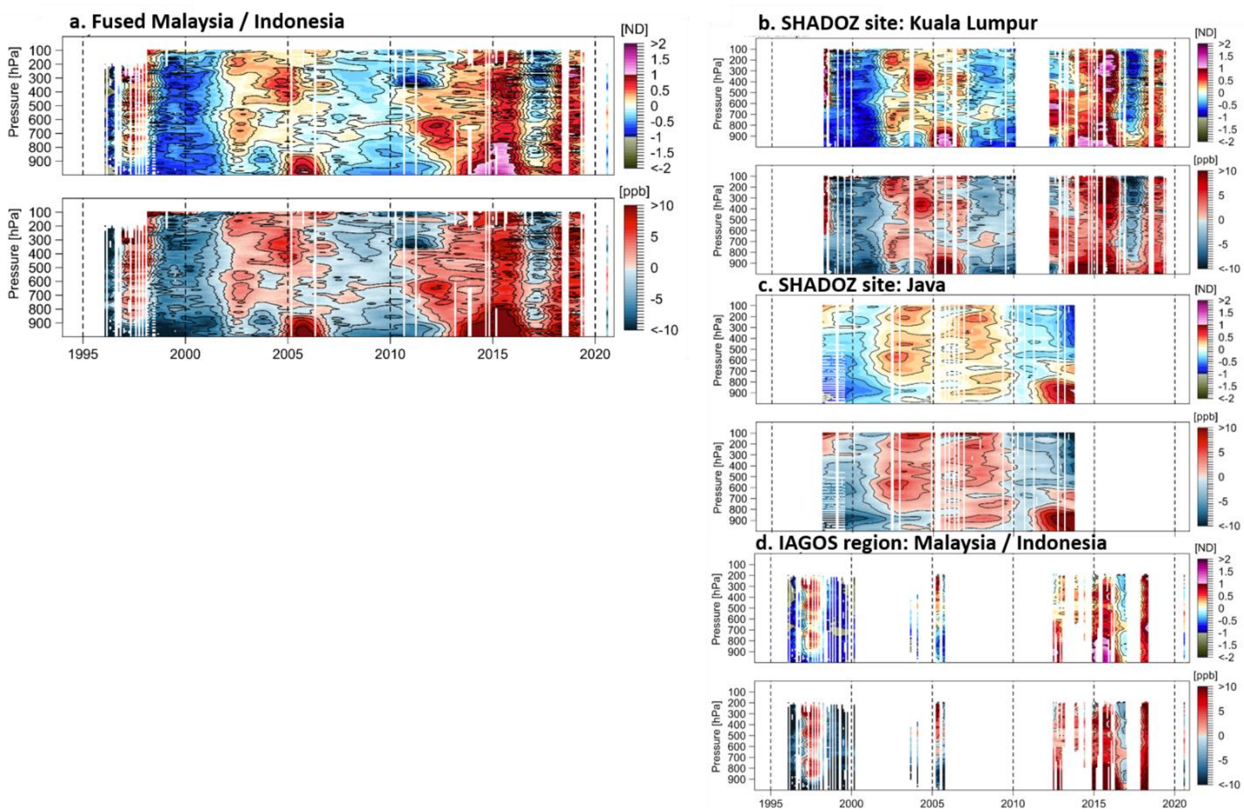

Figure S14. Same as Figure S12 but above Malaysia/Indonesia. The SHADOZ individual site used for the fused data is Kuala Lumpur and Watukosek (Java).

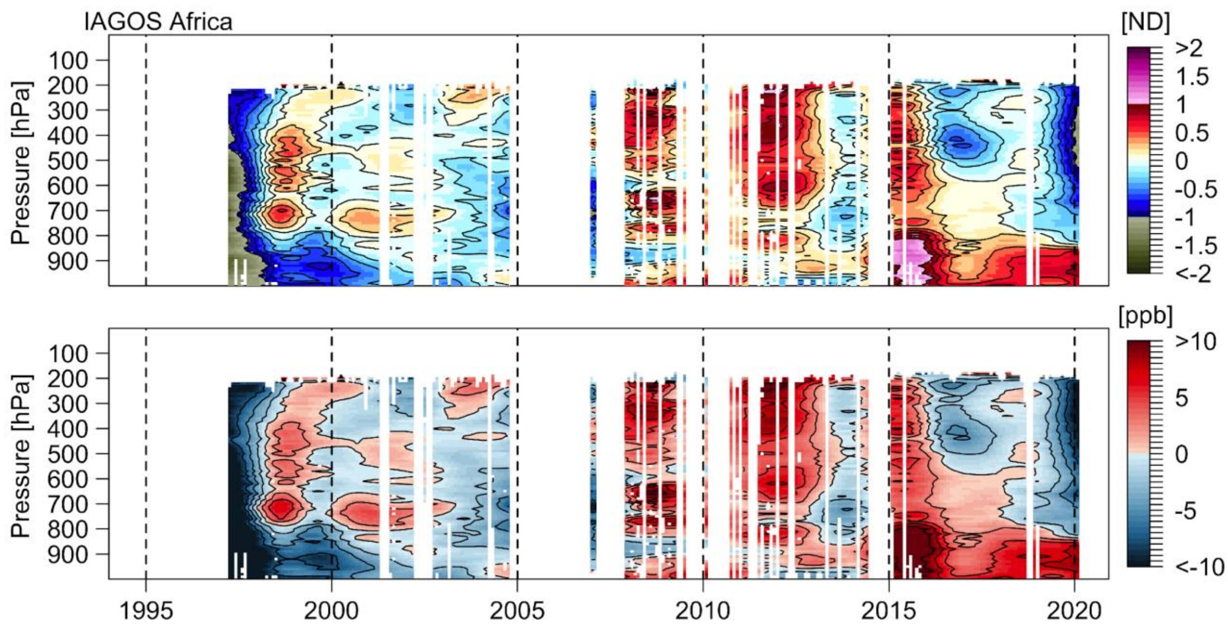

Figure S15. Same as Figure S12 but above western Africa. There are no SHADOZ data available in this region. We use only IAGOS data.

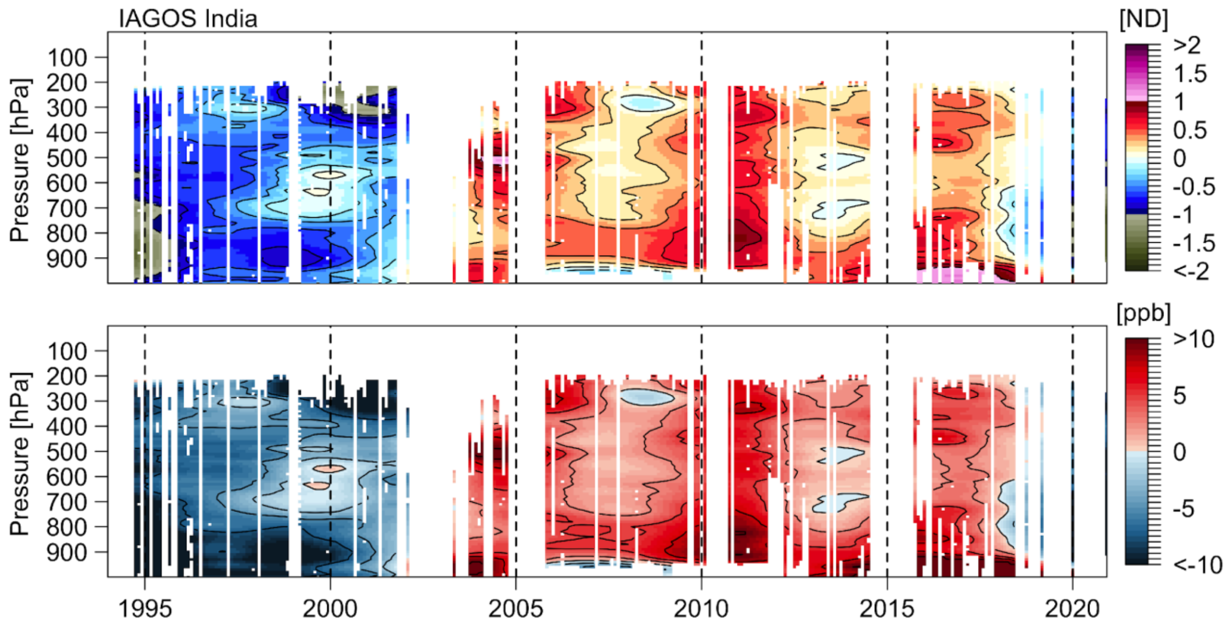

Figure S16. Same as Figure S12 but above India. There are no SHADOZ data available in this region. We use only IAGOS data.

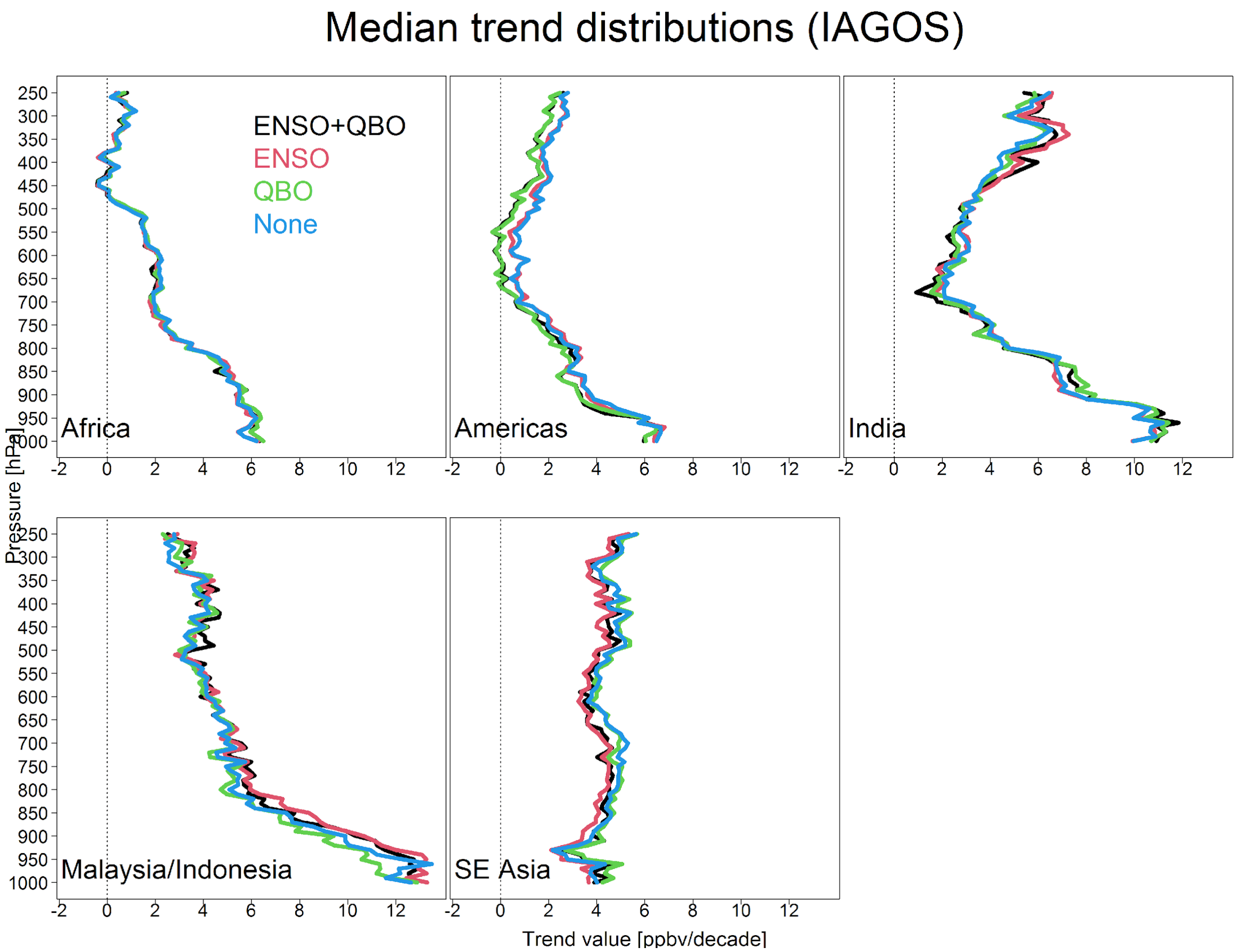

Figure S17. Vertical profiles of ozone trends (nmol mol^{-1}/decade) from a linear regression that considers climate variability such as ENSO (El Niño-Southern Oscillation) and QBO (quasi-biennial oscillation). The trends are reported over the five IAGOS regions: Africa, Americas, India, Malaysia/Indonesia and Southeast Asia.

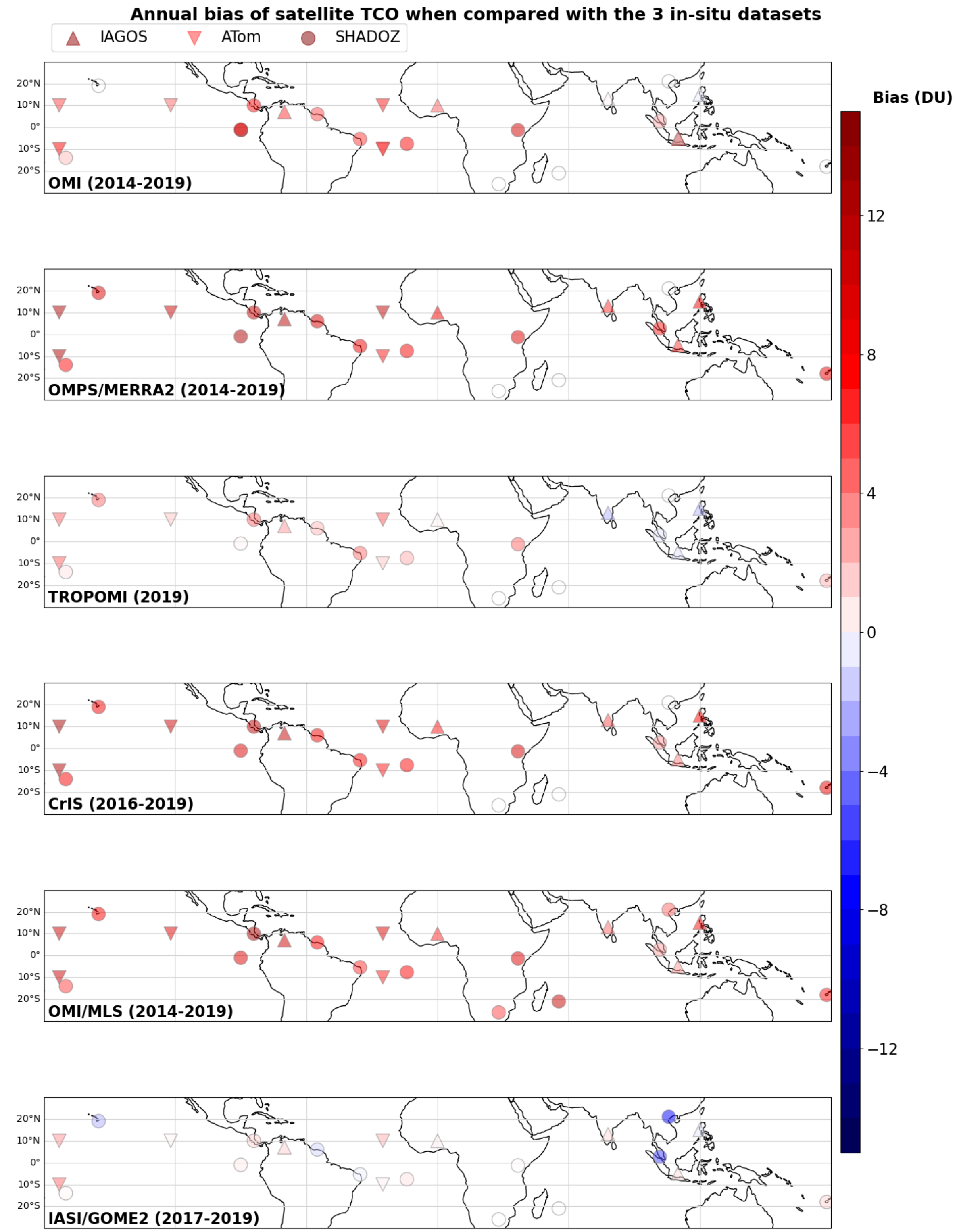

Figure S18. Absolute annual mean biases of tropical tropospheric column ozone (TTCO in DU) of the six satellite products: OMI (2014-2019), OMPS/MERRA2 (2014-2019), TROPOMI

(2019), CrIS (2018-2019), OMI/MLS (2014-2019) and IASI/GOME2 (2017-2019) against the three in situ TTCO up to 270 hPa: IAGOS (2014-2019), SHADOZ (2014-2019) and ATom (2016-2018).

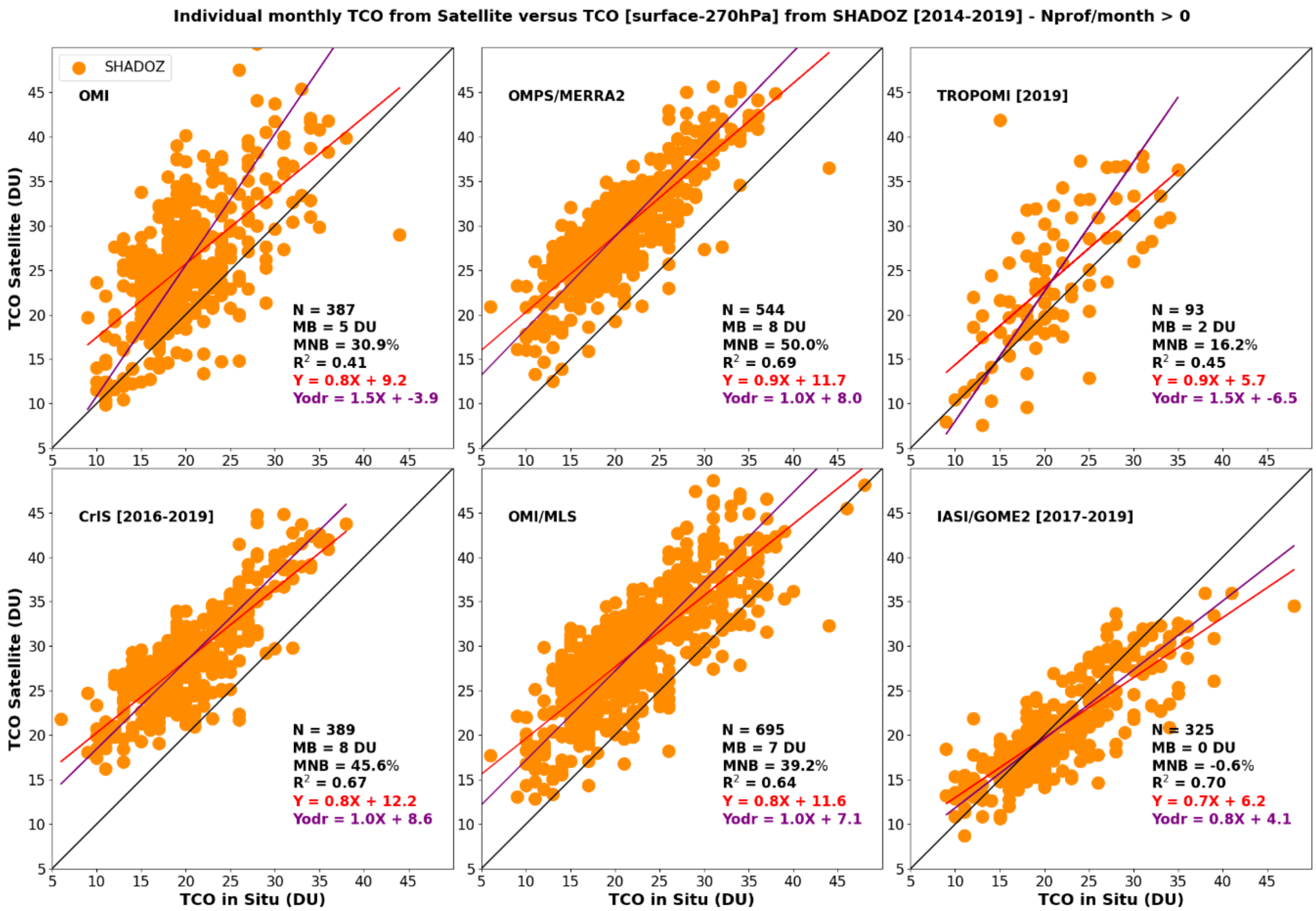

Figure S19. Similar to Figure 5 but the in situ TTCO is derived from integrating the column up to 270 hPa instead of 100 hPa.

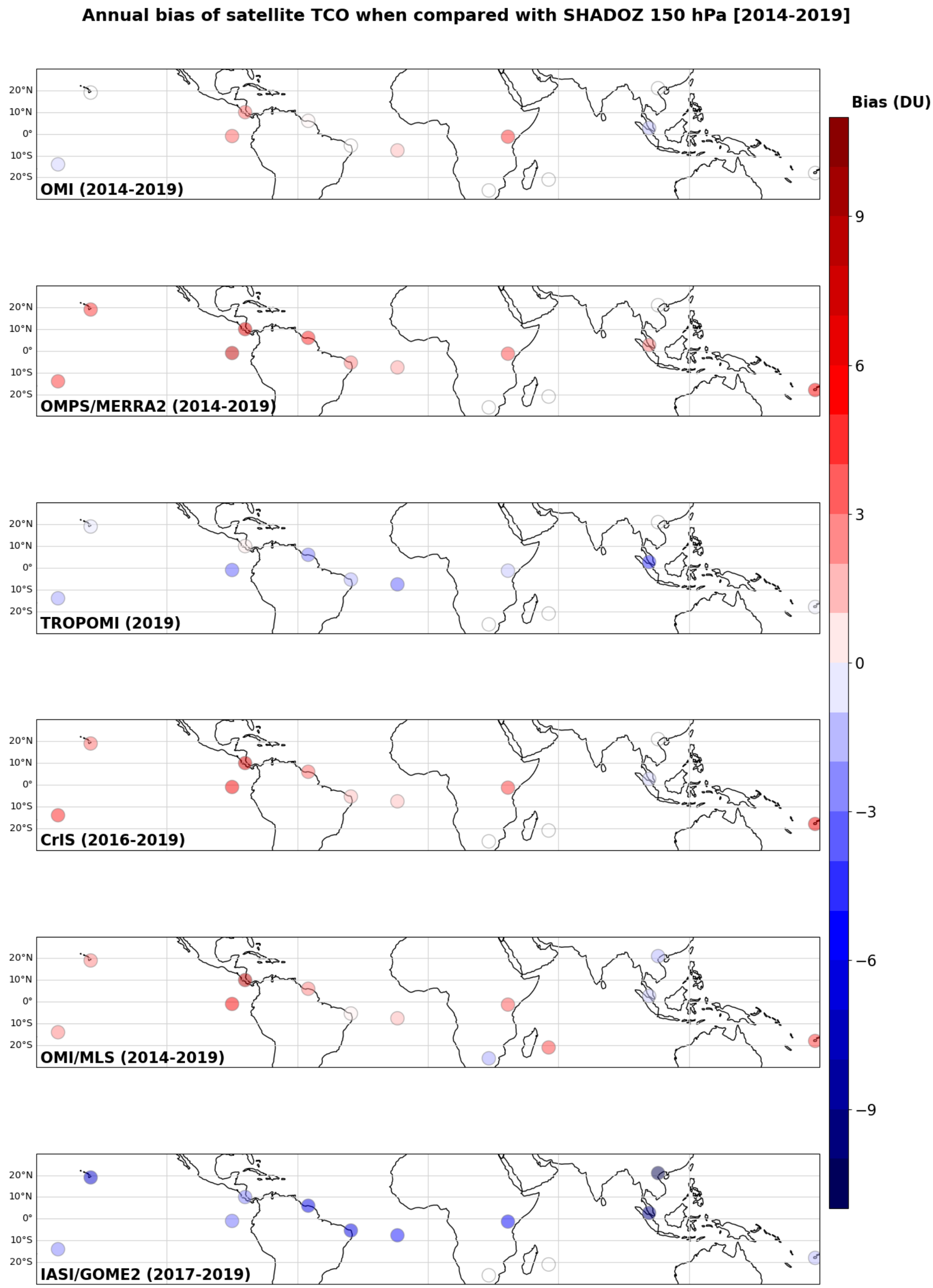

Figure S20. Same as Figure S13 but against SHADOZ only (TTCO up to 150 hPa).

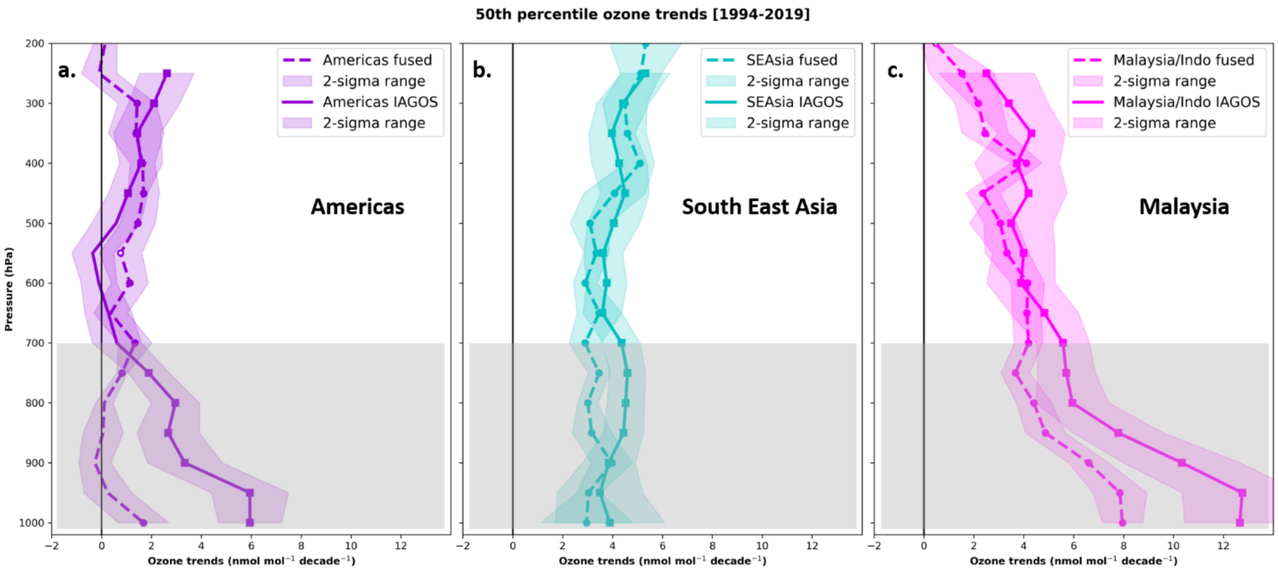

Figure S21. Vertical profiles of ozone trends (nmol mol^{-1} decade^{-1}) between 1994 and 2019, at 50 hPa vertical resolution. Fused (circles) and IAGOS only (squares) trends are calculated for the 3 out of the 5 IAGOS regions: Americas (a), Southeast Asia (b) and Malaysia/Indonesia (c) for which both IAGOS and SHADOZ data are available. Filled circles and squares indicate trends with p-values less than 0.05. Open circles indicate trends with p-values between 0.05 and 0.1. The zero-trend value is indicated with a vertical black line. The vertical range below 700 hPa is shaded grey to indicate that the fused trends are based on several sites and airports influenced by different local air masses. The 2-sigma values associated with the ozone trends are shown in shaded colors.

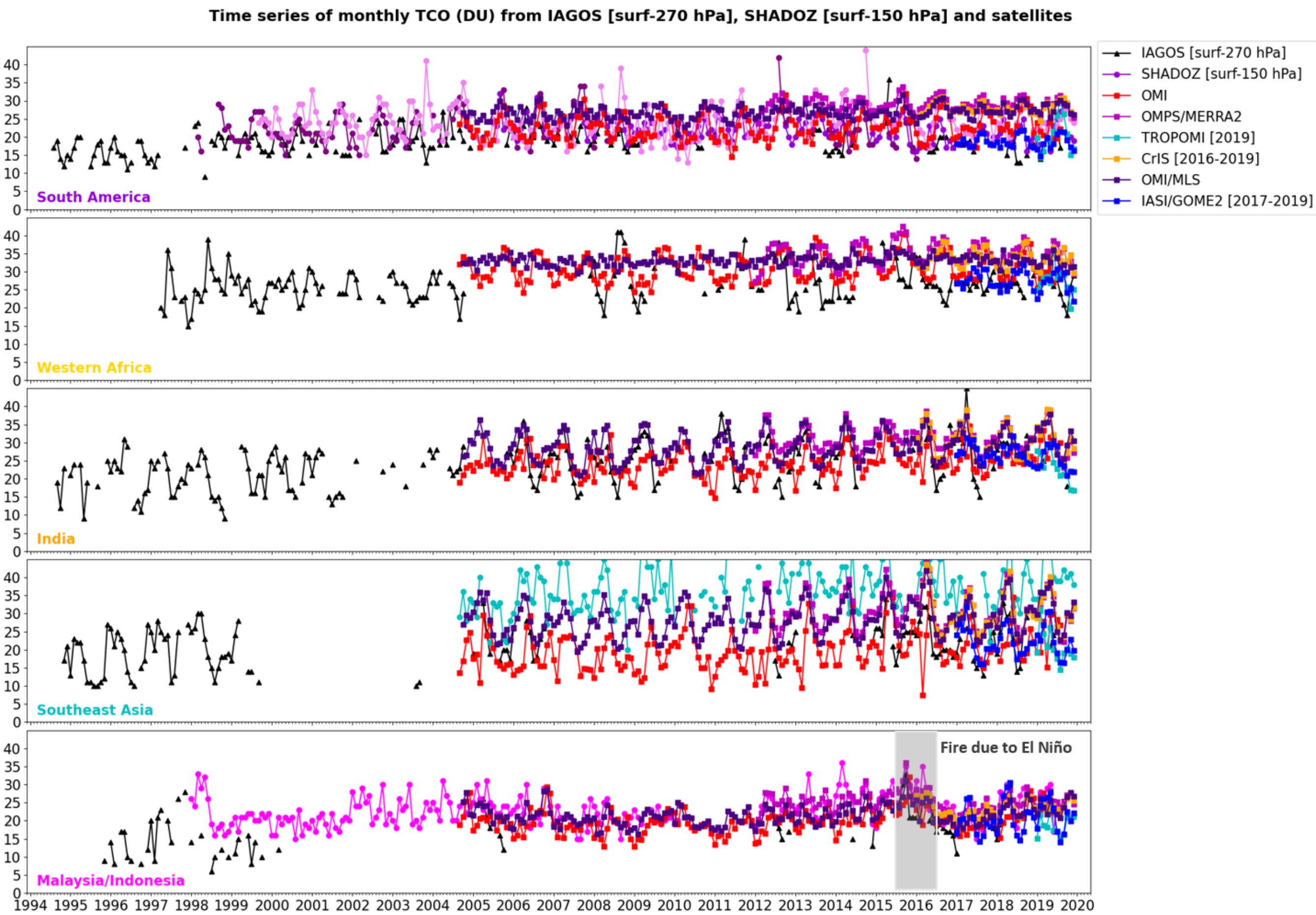

Figure S22. Time series of the monthly tropical tropospheric column ozone (TTCO) from IAGOS ozone profiles (TTCO: surface-270 hPa, black line with triangle markers), from SHADOZ ozone profiles (TTCO: surface-150hPa, colored lines with circle markers), and satellite data (colored line with square markers) extracted above the IAGOS regions. These monthly columns are not used to assess the trends reported in Table 1.

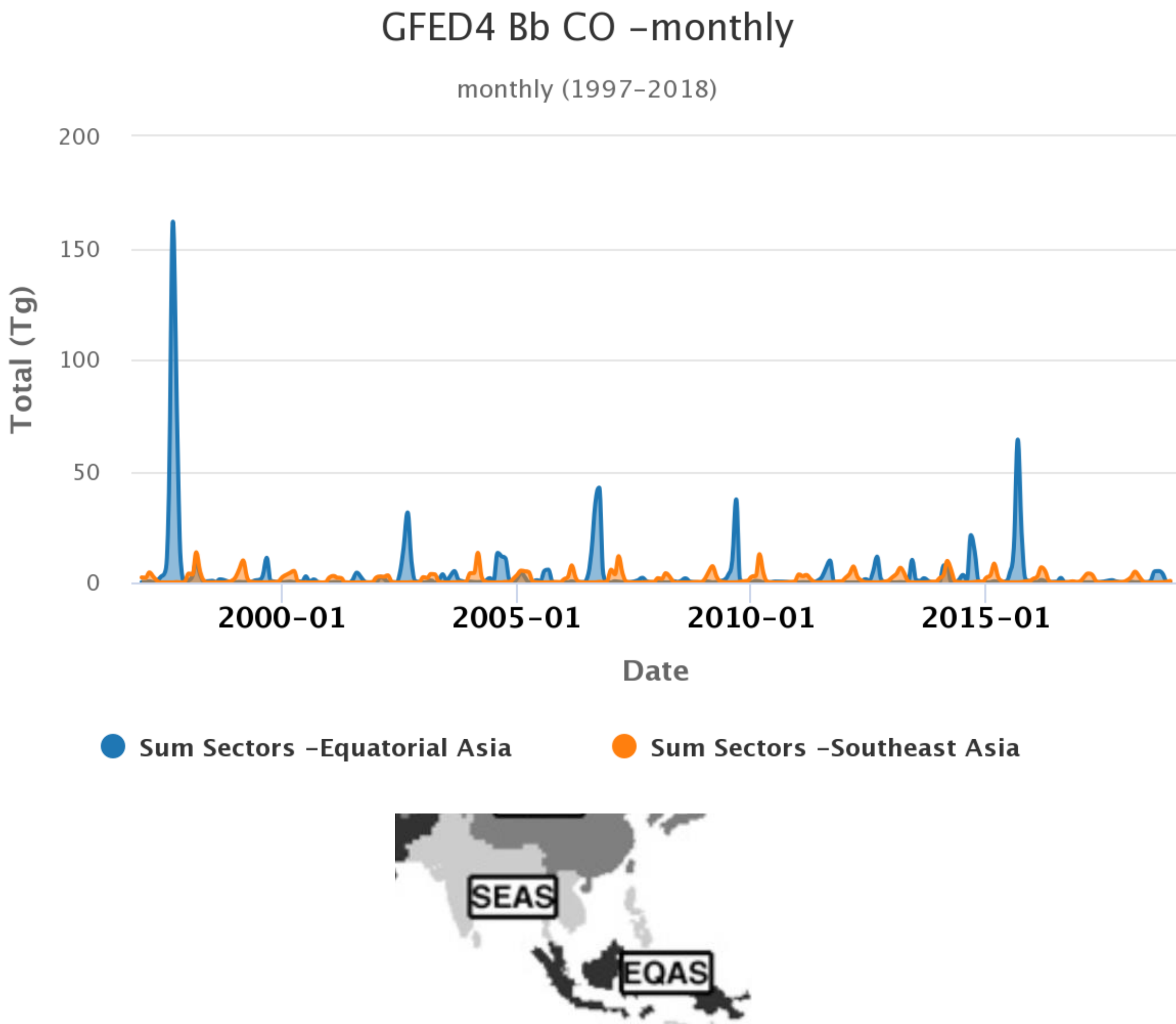

Figure S23. Time series of monthly emissions of CO in Tg due to biomass burning over two GFED source regions: Equatorial Asia (EQAS) and Southeast Asia (SEAS). *Source: ECCAD (https://eccad.aeris-data.fr/*, Darras et al., 2018*)*

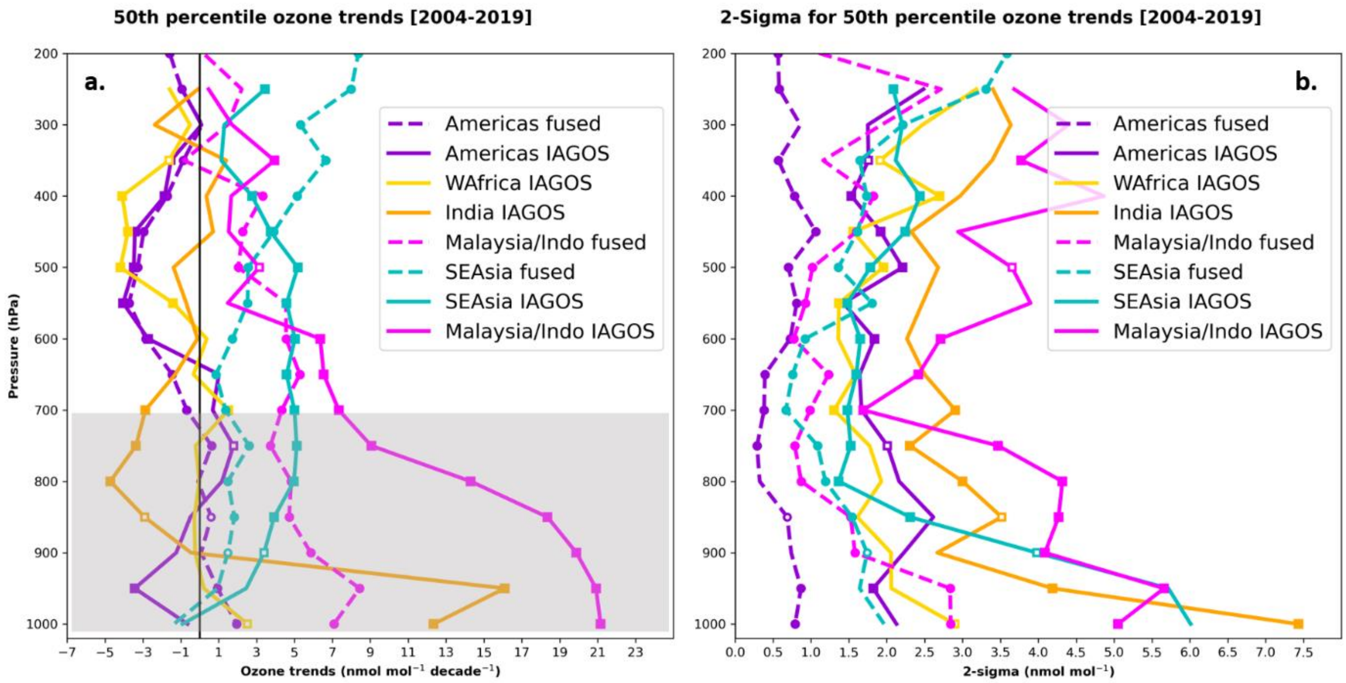

Figures S24. Vertical profiles of ozone trends (nmol mol^{-1} decade^{-1}) (panel a.) and the associated uncertainties (2-sigma, panel b.) between 2004 and 2019 with 50 hPa resolution. Trends are calculated for the 5 IAGOS regions in the tropics:
Americas, Western Africa, India, Southeast Asia and Malaysia/Indonesia. SHADOZ data are available for 3 out of the 5 IAGOS regions and fused trends (IAGOS + SHADOZ) were assessed.
Squares (IAGOS trends) or circles (fused trends) indicate trends with p values less than 0.05. Open squares or circles indicate trends with p values between 0.05 and 0.1. The zero-trend value is indicated with a vertical black bar. The vertical range below 700 hPa is colored in grey to indicate that the fused trends are based on several sites and airports influenced by different local air masses.

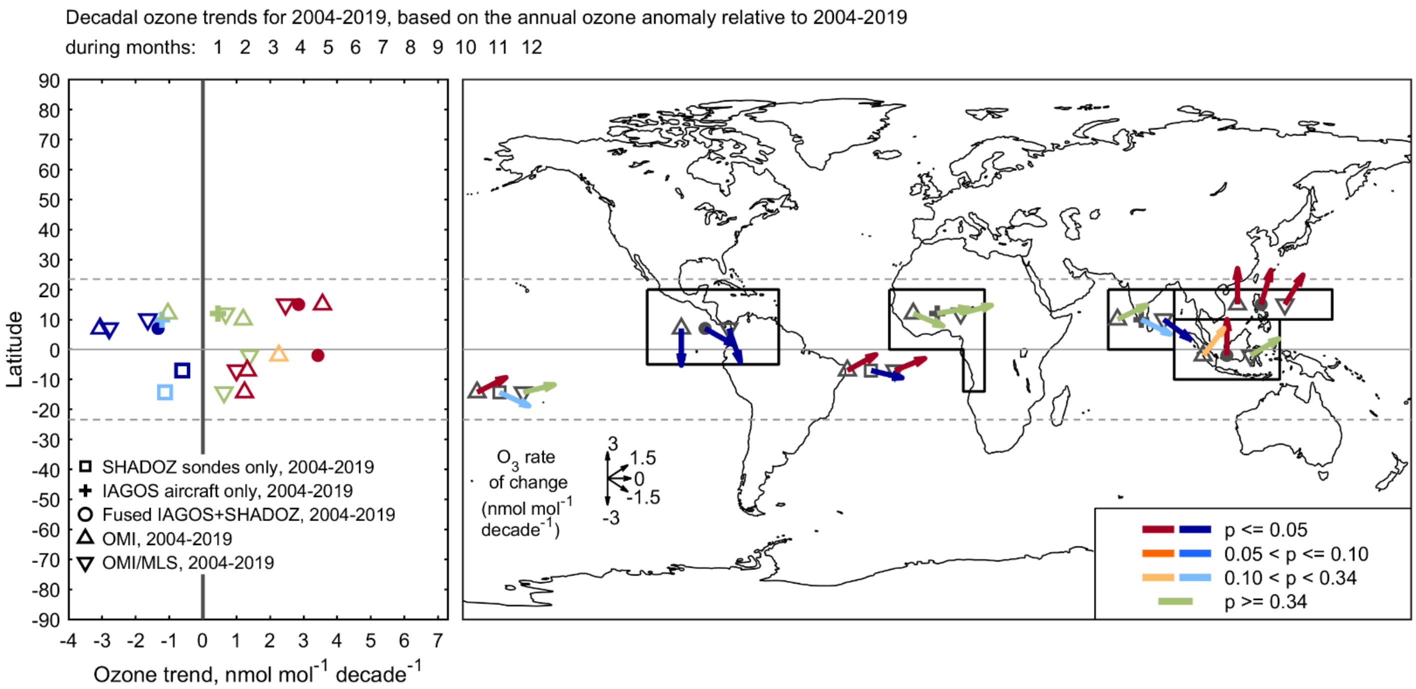

Figure S25. As in Figure 7 but the satellite sample sizes have been greatly reduced so that they only coincide with the specific months and grid-cells sampled by the IAGOS aircraft. Trends of tropical tropospheric column ozone (TTCO) in nmol mol^{-1} decade^{-1} between 2004 and 2019 from IAGOS (crosses), SHADOZ (squares), IAGOS fused with SHADOZ (circles), OMI (triangles up) and OMI/MLS (triangles down) above the five continental IAGOS regions (Americas, Africa, India, Southeast Asia and Malaysia/Indonesia) and two oceanic SHADOZ regions (Samoa and Natal + Ascension Island). The left panel shows the trends of ozone as a function of latitude. The right panel shows the trends of ozone on the map with the black rectangles demarcating the five IAGOS regions. On the map, the longitude of the crosses, circles, triangles and squares are arbitrary and the latitude is the mean latitude of the black rectangles or relative to the SHADOZ sites. The direction of the arrows shows the magnitude of the trends and the colors indicate the *p*-value. The TTCO trends from in situ data are calculated from the monthly TTCO between the surface and 100 hPa, except over India where IAGOS profiles are available between the surface and around 200 hPa. The TTCO trends from OMI and OMI/MLS are calculated from the monthly TTCO defined between the surface and around 102-105 hPa (Figure S1).

References

Chang, K.-L., Cooper, O. R., Gaudel, A., Petropavlovskikh, I., and Thouret, V.: Statistical regularization for trend detection: an integrated approach for detecting long-term trends from sparse tropospheric ozone profiles, Atmos. Chem. Phys., 20, 9915–9938, https://doi.org/10.5194/acp-20-9915-2020, 2020.

Chang, K. L., Cooper, O. R., Gaudel, A., Allaart, M., Ancellet, G., Clark, H., Godin-Beekmann, S., Leblanc, T., Van Malderen, R., Nédélec, P., and Petropavlovskikh, I.: Impact of the COVID-19 economic downturn on tropospheric ozone trends: An uncertainty weighted data synthesis for quantifying regional anomalies above western North America and Europe, AGU Advances, 3, e2021AV000542, https://doi.org/10.1029/2021AV000542, 2022.

Chang, K.-L., Schultz, M. G., Koren, G., and Selke, N.: Guidance note on best statistical practices for TOAR analyses, https://igacproject.org/activities/TOAR/TOAR-II (last access: 23 August 2023), 2023.

Darras, S., Granier, C., Liousse, C., Boulanger, D., Elguindi, N., and Le Vu, H.: The ECCAD database, version 2: Emissions of atmospheric Compounds & Compilation of Ancillary Data, IGAC Newsletter, 2018

De Mazière, M., Thompson, A. M., Kurylo, M. J., Wild, J. D., Bernhard, G., Blumenstock, T., Braathen, G. O., Hannigan, J. W., Lambert, J.-C., Leblanc, T., McGee, T. J., Nedoluha, G., Petropavlovskikh, I., Seckmeyer, G., Simon, P. C., Stein brecht, W., and Strahan, S. E.: The Network for the Detection of Atmospheric Composition Change (NDACC): history, status and perspectives, Atmos. Chem. Phys., 18, 4935–4964, https://doi.org/10.5194/acp-18-4935-2018, 2018.

Fishman, J., Watson, C. E., Larsen, J. C., and Logan, J. A.: Distribution of tropospheric ozone determined from satellite data, J. Geophys. Res., 95, 3599–3617, https://doi.org/10.1029/JD095iD04p03599, 1990.

Logan, J. A.: An analysis of ozonesonde data for the troposphere: Recommendations for testing 3-D models and development of a gridded climatology for tropospheric ozone, J. Geophys. Res. Atmos., 104, 16115–16149, 1999.

Saunois, M., Emmons, L., Lamarque, J.-F., Tilmes, S., Wespes, C., Thouret, V., and Schultz, M.: Impact of sampling frequency in the analysis of tropospheric ozone observations, Atmos. Chem. Phys., 12, 6757–6773, https://doi.org/10.5194/acp-12-6757-2012, 2012.

Sterling, C. W., Johnson, B. J., Oltmans, S. J., Smit, H. G. J., Jordan, A. F., Cullis, P. D., Hall, E. G., Thompson, A. M., and Witte, J. C.: Homogenizing and estimating the uncertainty in NOAA's long-term vertical ozone profile records measured with the electrochemical concentration cell ozonesonde, Atmos. Meas. Tech., 11, 3661–3687, https://doi.org/10.5194/amt-11-3661-2018, 2018.

Thompson, A. M., Witte, J. C., Sterling, C., Jordan, A., Johnson, B. J., Oltmans, S. J., Fujiwara, M., Vömel, H., Allaart, M., Piters, A., and Coetzee, G. J.: First reprocessing of Southern Hemisphere Additional Ozonesondes (SHADOZ) ozone profiles (1998–2016): 2. Comparisons with satellites and groundbased instruments, J. Geophys. Res.-Atmos., 122, 13000–13025, https://doi.org/10.1002/2017JD027406, 2017.

Torres, O., Bhartia, P. K., Jethva, H., and Ahn, C.: Impact of the ozone monitoring instrument row anomaly on the long-term record of aerosol products, Atmos. Meas. Tech., 11, 2701–2715, https://doi.org/10.5194/amt-11-2701-2018, 2018

Witte, J. C., Thompson, A. M., Smit, H. G., Fujiwara, M., Posny, F., Coetzee, G. J., Northam, E. T., Johnson, B. J., Sterling, C.W., Mohamad, M., and Ogino, S. Y.: First reprocessing of Southern Hemisphere ADditional OZonesondes (SHADOZ) profile records (1998–2015): 1. Methodology and evaluation, J. Geophys. Res.-Atmos., 122, 6611–6636, 2017.

Witte, J. C., Thompson, A. M., Smit, H. G. J., Vömel, H., Posny, F., and Stübi, R.: First reprocessing of SouthernHemisphere Additional OZonesondesprofile records: 3. Uncertainty in ozone profile and total column, J. Geophys. Res.-Atmos., 123, 3243–3268, https://doi.org/10.1002/2017JD027791, 2018.

Ziemke, J. R., Chandra, S., and Bhartia, P. K.: Two new methods for deriving tropospheric column ozone from TOMS measurements: The assimilated UARS MLS/HALOE and convective-cloud differential techniques, J. Geophys. Res., 103, 22115–22127, 1998.

Ziemke, J. R., Chandra, S., Duncan, B. N., Froidevaux, L., Bhartia, P. K., Levelt, P. F., and Waters, J. W.: Tropospheric ozone determined from Aura OMI and MLS: Evaluation of measurements and comparison with the Global Modeling Initiative's Chemical Transport Model, J. Geophys. Res.-Atmos., 111, D19, https://doi.org/10.1029/2006JD007089, 2006

Ziemke, J. R., Oman, L. D., Strode, S. A., Douglass, A. R., Olsen, M. A., McPeters, R. D., Bhartia, P. K., Froidevaux, L., Labow, G. J., Witte, J. C., Thompson, A. M., Haffner, D. P., Kramarova, N. A., Frith, S. M., Huang, L.-K., Jaross, G. R., Seftor, C. J., Deland, M. T., and Taylor, S. L.: Trends in global tropospheric ozone inferred from a composite record of TOMS/OMI/MLS/OMPS satellite measurements and the MERRA-2 GMI simulation, Atmos. Chem. Phys., 19, 3257–3269, https://doi.org/10.5194/acp-19-3257-2019, 2019.